Science and Technology of Advanced Materials

ISSN: (Print) (Online) Journal homepage: https://www.tandfonline.com/loi/tsta20

Synthesis of mesoscopic particles of multi-component rare earth permanent magnet compounds

T. Thuy Trinh, Jungryang Kim, Ryota Sato, Kenshi Matsumoto & Toshiharu Teranishi

To cite this article: T. Thuy Trinh, Jungryang Kim, Ryota Sato, Kenshi Matsumoto & Toshiharu Teranishi (2021) Synthesis of mesoscopic particles of multi-component rare earth permanent magnet compounds, Science and Technology of Advanced Materials, 22:1, 37-54, DOI: 10.1080/14686996.2020.1862630

To link to this article: https://doi.org/10.1080/14686996.2020.1862630

Published online: 22 Jan 2021.

SCIENCE AND TECHNOLOGY OF ADVANCED MATERIALS
2021, VOL. 22, NO. 1, 37–54
https://doi.org/10.1080/14686996.2020.1862630

Taylor & Francis
Taylor & Francis Group

FOCUS ISSUE REVIEW

OPEN ACCESS Check for updates

Synthesis of mesoscopic particles of multi-component rare earth permanent magnet compounds

T. Thuy Trinh, Jungryang Kim, Ryota Sato, Kenshi Matsumoto and Toshiharu Teranishi

Institute for Chemical Research, Kyoto University, Uji, Kyoto, Japan

ABSTRACT

Multielement rare earth (R)–transition metal (T) intermetallics are arguably the next generation of high-performance permanent magnetic materials for future applications in energy-saving and renewable energy technologies. Pseudobinary $Sm_2Fe_{17}N_3$ and $(R,Zr)(Fe,Co,Ti)_{12}$ (R = Nd, Sm) compounds have the highest potential to meet current demands for rare-earth-element-lean permanent magnets (PMs) with ultra-large energy product and operating temperatures up to 200°C. However, the synthesis of these materials, especially in the mesoscopic scale for maximizing the maximum energy product ($(BH)_{max}$), remains a great challenge. Nonequilibrium processes are apparently used to overcome the phase-stabilization challenge in preparing the R–T intermetallics but have limited control of the material's microstructure. More radical bottom-up nanoparticle approaches based on chemical synthesis have also been explored, owing to their potential to achieve the desired composition, structure, size, and shape. While a great achievement has been made for the $Sm_2Fe_{17}N_3$, progress in the synthesis of $(R,Zr)(Fe,Co,Ti)_{12}$ magnetic mesoscopic particles (MMPs) and R–T/T exchange-coupled nanocomposites (NCMs) with substantial coercivity (H_c) and remanence (M_r), respectively, remains marginal.

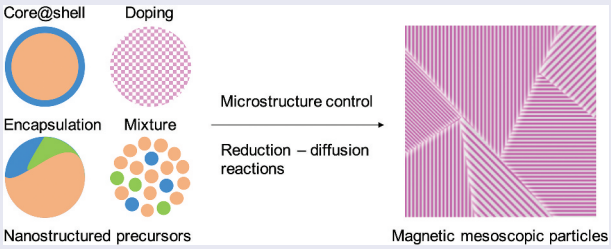

ARTICLE HISTORY
Received 20 September 2020
Revised 6 December 2020
Accepted 7 December 2020

CLASSIFICATION
102 Porous / Nanoporous / Nanostructured materials; 103 Composites, 106 Metallic materials; 203 Magnetics / Spintronics / Superconductors; 301 Chemical syntheses / processing

1. Introduction

The current high-end permanent magnet, $Nd_2Fe_{14}B$ ($P4_2/mnm$) compound, has a relatively low Curie temperature T_c of 313°C [1,2] and, since its sintered magnet ($Nd_2Fe_{14}B$: 0.982 vol.%, O_2: 600 ppm, grain orientation: 0.991) has reached the room-temperature $(BH)_{max}$ of 474 kJm^{-3} [3], approaching the theoretical limit of 520 kJm^{-3}, high-performance permanent magnetic compounds that outperform the $Nd_2Fe_{14}B$ and operate at elevated temperatures (typically 200°C) for highly efficient electric motors and generators are ever-increasing demand [4–8]. Uniaxial magnetocrystalline multielement R–T intermetallics are arguably the exclusive candidates that can process ultra-large intrinsic magnetic properties, where strong spin-orbit coupling (SOC) of 4*f* electrons of R sublattice originates large uniaxial magnetocrystalline anisotropy field, H_a, and large magnetic moment and strong exchange interactions of 3*d* electrons of T sublattice result in large saturation magnetization, M_s, and high T_c, respectively, [9,10]. Among them, R_2T_{17} (Th_2Zn_{17}-type, *R*-3*m*) and RT_{12} ($ThMn_{12}$-type, *I*4/*mmm*) compounds have the potential to meet current demands for rare-earth-element-lean PMs, owing to their intrinsic magnetic properties superior to those of the $Nd_2Fe_{14}B$ compound (Figure 1) [1,2,11–22].

Magnetism on the mesoscopic scale, which is known as micromagnetism, exhibits particularly rich extrinsic behavior. H_c is an extrinsic property of crucial importance in permanent magnetism and is governed by the real structure of materials under Brown's paradox [23,24]: H_c is reduced to αH_a by defects, where the factor α ($0 \le \alpha < 1$) describes microstructural details [25–29]. The MMPs, especially magnetic nanoparticles (MNPs), are an important class of magnet building blocks that can be used to fabricate high-performance anisotropic PMs [30–32]. Their unique feature is the size-dependent coercivity: H_c of a single-domain grain increases beyond the superparamagnetic critical size (D_{sp}) as $H_c \sim 1 - (D_{sp}/D)^{3/2}$, reaches the

CONTACT Toshiharu Teranishi teranisi@scl.kyoto-u.ac.jp Institute for Chemical Research, Kyoto University, Uji, Kyoto 611-0011, Japan

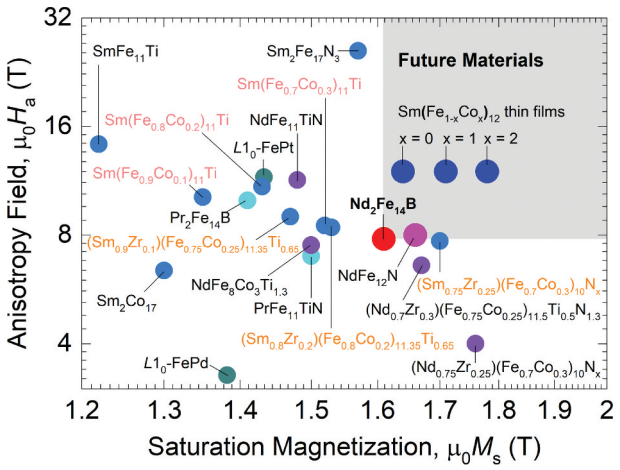

Figure 1. Room-temperature intrinsic magnetic properties of up-to-date representative compounds. The $Sm(Fe_{1-x}Co_x)_{12}$ and $NdFe_{12}N$ compounds are in the form of thin film; the other compounds are in the form of micropowders. Data are incorporated with references [1,11–22].

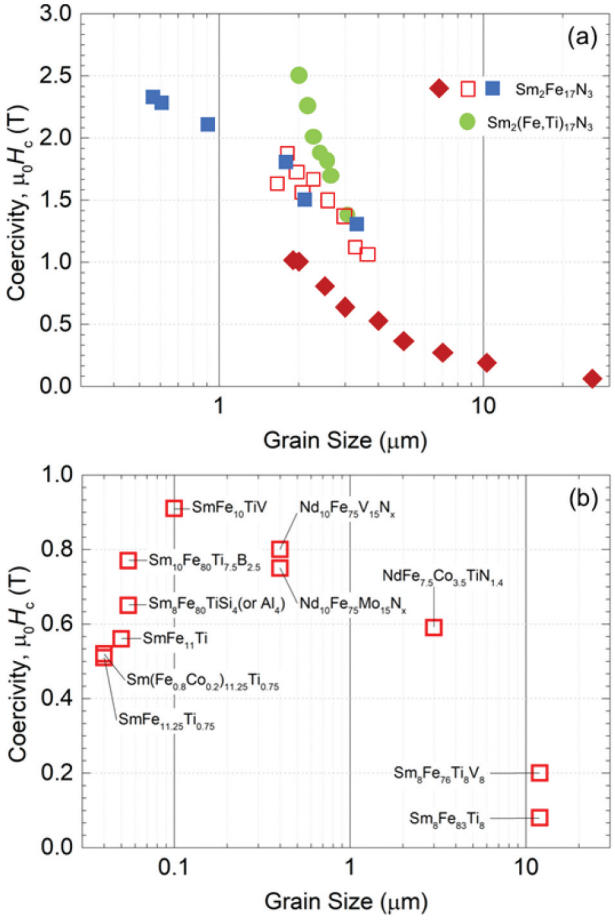

Figure 2. Grain size dependence of room-temperature coercivity. (a) $Sm_2Fe_{17}N_3$ compounds. (b) $R(Fe,M)_{12}X_x$ (R = Nd, Sm; M = Ti, V, Co, Mo, Al, Si: phase stabilizing elements; X = N, B) compounds. (a) Reprinted with permission from [39]. Copyright 2020 Elsevier. (b) Data are incorporated with references [40–50].

maximum at the single-domain critical size (D_{sd}) given by $D_{sd} \approx 72\sqrt{A_{ex}K_1}/\mu_0 M_s^2$ where A_{ex} is the exchange stiffness and K_1 is the first anisotropy constant, and then decreases as $H_c \sim 1/D^n$, provided that the grain has a strong cubic anisotropy [33–36]. The grain-size dependent coercivities of representative R_2T_{17} and RT_{12} compounds are named a few and shown in Figure 2 [37–50]. Owing to the phase-stabilization challenges, control over the microstructure of R–T multielement materials is still a non-trivial task, though the R–T permanent magnetic materials have been established since 1960s [51] and the $Nd_2Fe_{14}B$ compound has been utilized since its discovery in 1984 [52–55].

Synthesis of multielement R–T intermetallics, especially the RT_{12} compound, is very challenging due to their complex crystal structure, desired phases formed in narrow compositions and at very high temperatures (700–1200°C), and poor chemical stability in the air environment [56–60]. In general, the R–T intermetallics with equilibrium phases can be synthesized by equilibrium processes under the framework of their equilibrium phase diagrams, such as cooling of the alloying liquid with a very low cooling rate and annealing of the as-casting ingots at elevated temperatures for a time as long as possible. The later process utilizing arc-melting or induction-melting and subsequent annealing is convenient to synthesize the intermetallics [12,13,16–19,22,37,58,59,61]. However, the equilibrium processes often lead to the formation of impurities because the strict equilibrium conditions to give pure phases are hardly realized, and/or the metals R and T can easily form several equilibrium phases, thus make the microstructure, especially the size, less controllable. In contrast, the nonequilibrium processes are appropriate for synthesizing not only metastable compounds but also the intermetallics with desired crystal structures free from impurities and a fine grain microstructure [61]. The most typical method is first to form the amorphous phase, followed by annealing at an appropriate temperature [14,40–50]. The annealing evolves the formation of metastable phases, which can be produced at various extreme nonequilibrium conditions, and the dynamical transformation between the metastable and the equilibrium phases, corresponding to the local free-energy minima. The differences between the crystallographic symmetries of the phases result in the differences in the local free-energy minima for the formation of the phases. Other factors, such as the composition and the atomic binding energy, of course, also play an important role in the formation and stability of the phases. The descending sequence of the symmetries for the structures of the R–T compounds has been found as follows: Amorphous, $CaCu_5$-type ($P6/mmm$), $TbCu_7$-type ($P6/mmm$), Th_2Ni_{17}-type ($P6_3/mmc$), $Nd_2Fe_{14}B$-type ($P4_2/mnm$), $ThMn_{12}$-type ($I4/mmm$), Th_2Zn_{17}-type (R-$3m$), and $Nd_3(Fe,Ti)_{29}$-type (A_2/m) [56,57,61]. The differences

between the free-energy minima for the formation of the last five equilibrium phases in the sequence may be quite small, depending on the composition of alloys and the condition of the synthetic process, and, thus only one equilibrium phase usually forms as the final one under a given condition of compositions and processes [61]. The $CaCu_5$-type (*P6/mmm*) structure with the highest symmetry among those of the R–T metastable and equilibrium phases is the basic one from which the structures of various R–T compounds can be derived by replacements of the R atoms with a pair of T atoms, which is known as dumbbell atoms, as follows [56,57]:

$$2RT_5 - R + 2T = RT_{12}(I4/mmm),$$
$$3RT_5 - R + 2T = R_2T_{17}(R\text{-}3m \text{ or } P6_3/mmc),$$
$$5RT_5 - 2R + 4T = R_3T_{29}(A_2/m).$$

For most of the R–T compounds, the metastable $CaCu_5$-type phases may form in a narrow temperature range and, thus, are hardly observed experimentally. The formation of the $CaCu_5$-type phases can be observed by careful annealing with a very slow heating rate for a short time [46], whereas the metastable $TbCu_7$-type phases form in a sufficiently wide temperature range to be observed in various synthetic processes [14,40,43]. In practice, the metastable compounds usually crystallize at annealing temperatures slightly higher than the crystallization temperature of the amorphous phase, and subsequently can be dynamically transformed into more stable compounds at higher annealing temperatures [61]. Therefore, the choice of the appropriate annealing temperatures under a given condition of compositions and processes is essential to promote the formation of the desired intermetallic compounds. The following processes are those based on the method above: mechanical alloying; mechanical milling including high-energy ball milling (HEBM) and surfactant-assisted ball milling (SABM); rapid quenching/melt-spinning; hydrogenation disproportionation desorption recombination (HDDR) [61]. They are popularly adopted for the massive production of fine powders, although they have limited control of the microstructure of materials. DC magnetron sputtering nonequilibrium process is often used to fabricate metastable RT_{12} films [15,20]. Solid-state and solid-gas reactions are the other two powerful nonequilibrium processes for the synthesis of the metastable and intermetallic compounds [19,37–39], and they are further discussed hereinafter. Among bottom-up synthetic approaches, chemical synthesis is the most versatile method for the preparation of MMPs with controllable composition, structure, size, and shape [30–32,62]. Recent advances in the solution-phase synthesis of MNPs followed by the solid-state reaction have overcome the phase stabilization challenges in preparing R–T intermetallics, leading to the successful synthesis of some binary R–T MMPs (e.g., $SmCo_5$, Sm_2Co_{17}) with ultra-large room-temperature H_c [62,63]. Herein we present an overview of our ongoing research in the context of other recent developments in the chemical synthesis of the most challenging multielement pseudobinary R_2T_{17} and RT_{12} intermetallics with an emphasis on grain size and composition control. This review covers the basis behind the use of nanoparticles (NPs) as precursors for the microstructure control of MMPs and presents the most recent results of $Sm_2Fe_{17}N_3$ and $(R,Zr)(Fe,Co,M)_{12}$ (R = Nd, Sm; M = Ti, V, Cr, Mn, Co, Mo, W, Al, Si, Ga) MMPs. The review also summarizes the efforts in the chemical synthesis of magnetically hard/soft exchange-coupled R–T/T NCMs.

2. Synthesis of nanostructured precursors

The high negative reduction potentials of R cations, a large difference in reduction potentials of R and T cations, and high chemical instability of R metals make it impossible to directly synthesize R–T intermetallics by solution-phase chemical reactions. An alternative chemical synthetic approach is to first synthesize nanostructured precursors, which are chemically stable and readily synthesized by solution-phase reactions, followed by R–D reactions of the precursors. Monodisperse nanostructured precursors with controllable composition, size, and shape are an important key to determine the microstructure of MMPs, and they are advantageous depending on their structural fashions such as core@shell, encapsulated, doped, or mixed oxide NPs.

The core@shell nanostructures composed of T metal or T oxide (T–O) cores and R oxide (R–O) shells, namely T/T–O@R–O NPs hereinafter, are usually synthesized *via* a two-step reaction: the T or T–O NPs are firstly synthesized, followed by the deposition of R–O over the surface of the T or T–O NPs. The Co (*Fm*-3*m*) and amorphous Fe NPs with particle sizes of < 10 nm were readily synthesized by thermal decomposition of $Co_2(CO)_8$ and $Fe(CO)_5$, respectively, as reported by Sun and co-workers [64,65]. The Co ($P6_3/mmc$) nanorods with the length in the range of 200–300 nm and the average diameter of 20 nm could be synthesized by using a Ru-catalyzed solvothermal reaction of cobalt laurate in the presence of hexadexylamine in 1,2-butanediol [66]. Amorphous Fe nanospheres with a particle size of 200 nm were synthesized by Carpenter and co-workers [67], where $FeSO_4$ was reduced to Fe by $NaBH_4$ at room temperature in the presence of sodium citrate. A series of Fe–O NPs with tunable sizes in a wide range from *ca*. 10 nm to several hundred nanometers were also successfully synthesized by the following procedures. Wüstite FeO (*Fm*-3*m*) NPs were synthesized by reductive thermal decomposition of $Fe(acac)_3$ (acac = acetylacetonate) with oleic acid (OA) and oleylamine (OAm); their sizes were tuned from 14 to 100 nm by controlling the reaction temperatures [68]. Magnetite Fe_3O_4 (*Fd*-3*m*)

nanocubes were synthesized by thermal decomposition of $Fe(acac)_3$ in the presence of OA in benzyl ether solvent at 290°C [69]; their sizes were tuned from 20 to 200 nm by varying the OA concentration, as shown in Figure 3 [70]. Hyeon and co-workers developed the ultra-large-scale synthesis of smaller Fe_3O_4 nanospheres with tunable sizes in the range of 5–20 nm by thermal decomposition of Fe(III) oleate in various solvents with different boiling points [71]. The reactivity of nanostructured precursors toward the following R–D reaction can be tailored by adopting NPs with different shapes as the surface energy can govern the interdiffusion of metal atoms. For this purpose, Fe_3O_4 (*Fd*-3*m*) NPs with rationally-controlled shapes from a cube, truncated cube, cuboctahedron, truncated octahedron, to octahedron were prepared by varying the concentration of CPC (CPC = cetylpyridinium chloride), as shown in Figure 4 [70]. Once the transition metal core like the Co core was prepared, amorphous Sm–O shell could be deposited by thermal decomposition of $Sm(acac)_3$ at 300°C in 1-octadecene solvent, as shown in Figure 5(a) [65,66]. The temperature rate was kept as low as 2°C min^{-1} to avoid homogeneous nucleation of

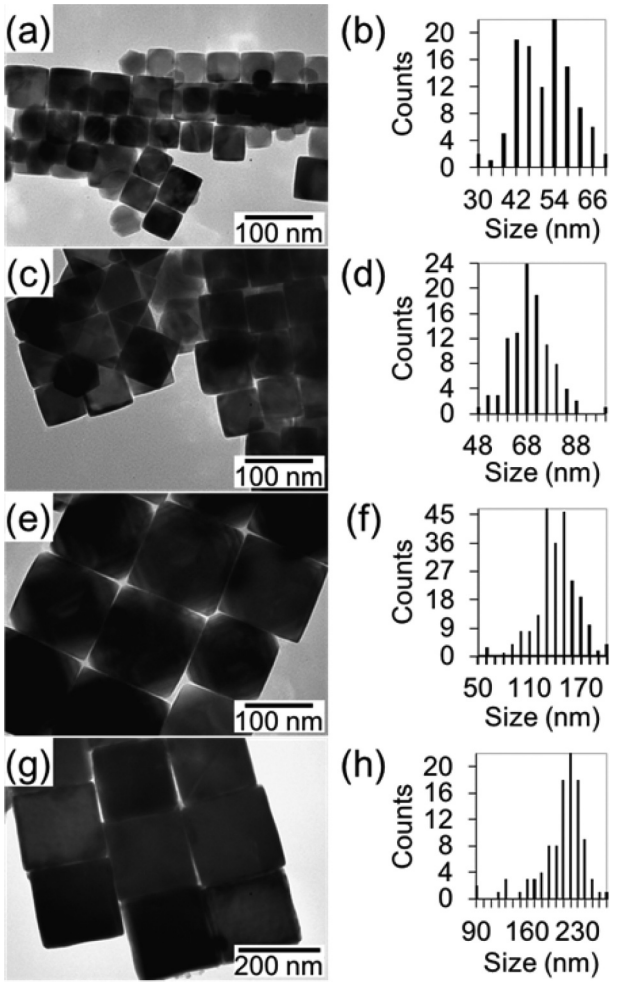

Figure 3. Size evolution of Fe_3O_4 (*Fd*-3*m*) NPs. (a,c,e,g) Transmission electron microscopy (TEM) images and (b,d,f,h) size distributions. Reprinted with permission from [70]. Copyright 2020 Wiley VCH.

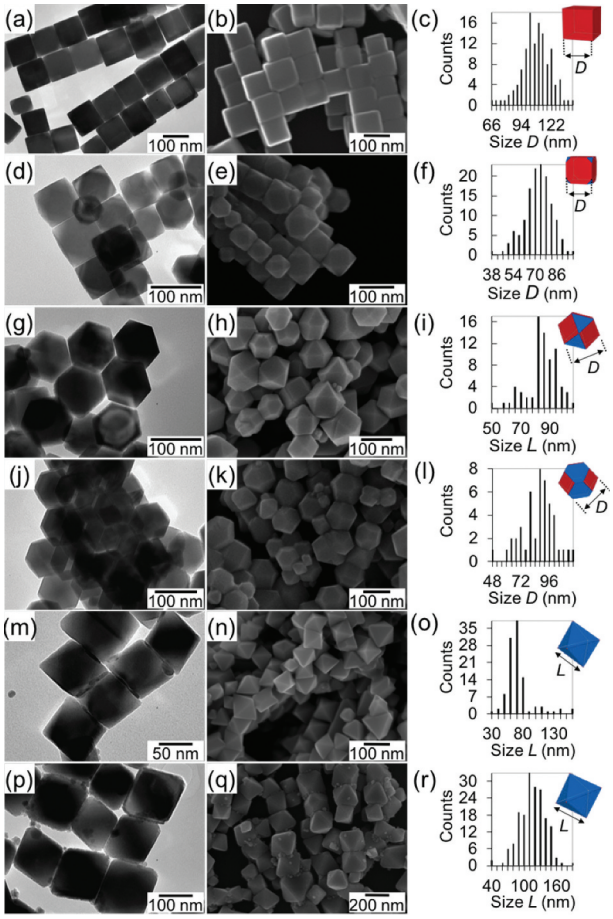

Figure 4. Shape evolution of Fe_3O_4 (*Fd*-3*m*) NPs: (a–c) cubes, (d–f) truncated cubes, (g–i) cuboctahedra, (j–l) truncated octahedra, (m–o) octahedra with small size, and (p–r) octahedra with large size. (a,d,g,j,m,p) TEM images, (b,e,h,k,n,q) Scanning electron microscopy (SEM) images, and (c,f,i,l,o,r) size distributions. Insets show the {100} and {111} planes in red and blue, respectively. Reprinted with permission from [70]. Copyright 2020 Wiley VCH.

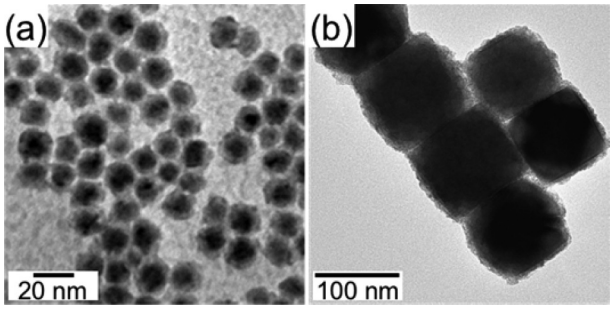

Figure 5. Chemically-synthesized core@shell nanostructured precursors. (a,b) TEM images of Co@Sm–O (Co core: *Fm*-3*m*, 8 nm; Sm:Co = 1:4.3 at%) (a) and Fe_3O_4@Sm–O (Fe_3O_4 core: *Fd*-3*m*, 79 nm; Sm:Fe = 1:11.5 at%) (b). (a) Reprinted with permission from [65]. Copyright 2020 Wiley VCH. (b) Reproduced with permission from [72]. Copyright 2020 the Chemical Society of Japan.

particulate Sm–O NPs. The method has been successfully extended to synthesize Fe_3O_4@Sm–O NPs, as shown in Figure 5(b) [72]. The molar ratio of Fe to Sm could be tuned by adjusting relative amounts of $Sm(acac)_3$ and Co or Fe_3O_4 NPs.

The T/T–O@R–O nanostructures are highly desirable because their size can be fully tuned in the mesoscopic scale from a few nanometers to one micrometer by well-established solution chemical synthetic methods. However, this strategy has succeeded rather in binary R–T MMPs [65,66]; it may be inappropriate for higher-multielement R–T MMPs since the synthetic process involves multi-step reactions giving a very low overall yield and the R/T ratio is not well-controlled. For better control of the R–T composition and full access to the control of particle size, the encapsulated nanostructures, where R–O and T–O in crystalline and/or amorphous forms are co-precipitated within one nanostructure (namely RT–O NPs hereinafter), can be used as precursors. The SmCo-O (7 nm) NPs were synthesized by thermal decomposition of $Sm(OAc)_3$ and $Co(OAc)_2$ (OAc = acetate) by Sun and co-workers, as shown in Figure 6(a) [73]. We successfully extended this method to synthesize multi-element NPs, *e.g.*, Sm–O, Zr–O, and Ti–O encapsulated $CoFe_2O_4$ (*Fd*-3*m*) NPs (5 nm), which will be reported in the forthcoming paper. Besides these, the Sm(Co or Fe)–O NPs with tunable sizes in the range of 60–220 nm and different morphologies were synthesized directly from thermal decomposition of $Sm(acac)_3$ and $Co/Fe(acac)_2$ (Figure 6(b–j)) [74] or SmCo–oleate complex (Figure 6(k–s)) [75]. The SmCo–O NPs with various morphologies, such as $Sm(OH)_3$–Co nanorods [76] or urchin-like [77], $Sm(OH)_3$–$Co(OH)_2$ nanoflakes [78,79], and SmCo–O nanofibers [80,81], could be successfully obtained by sonification [76], hydro/solvothermal reaction [77–79], and electrospinning [80,81]. Once the R amounts in these encapsulated nanostructures are under the critical concentration for the solid-solution formation, the R-doped T–O nanostructures can be synthesized by using procedures which are similar to the above [81–85]. A series of R-doped Fe_2O_3 or Fe_3O_4 (R = Sm, Eu, Gd, Tb, Ho, Er, Y) NPs with different shapes and particle sizes tuned in the range of 5 nm–1 μm could be obtained by thermal decomposition [82,84], hydrothermal reaction [85], and ultrasonication [86]. These precursors with R compositions

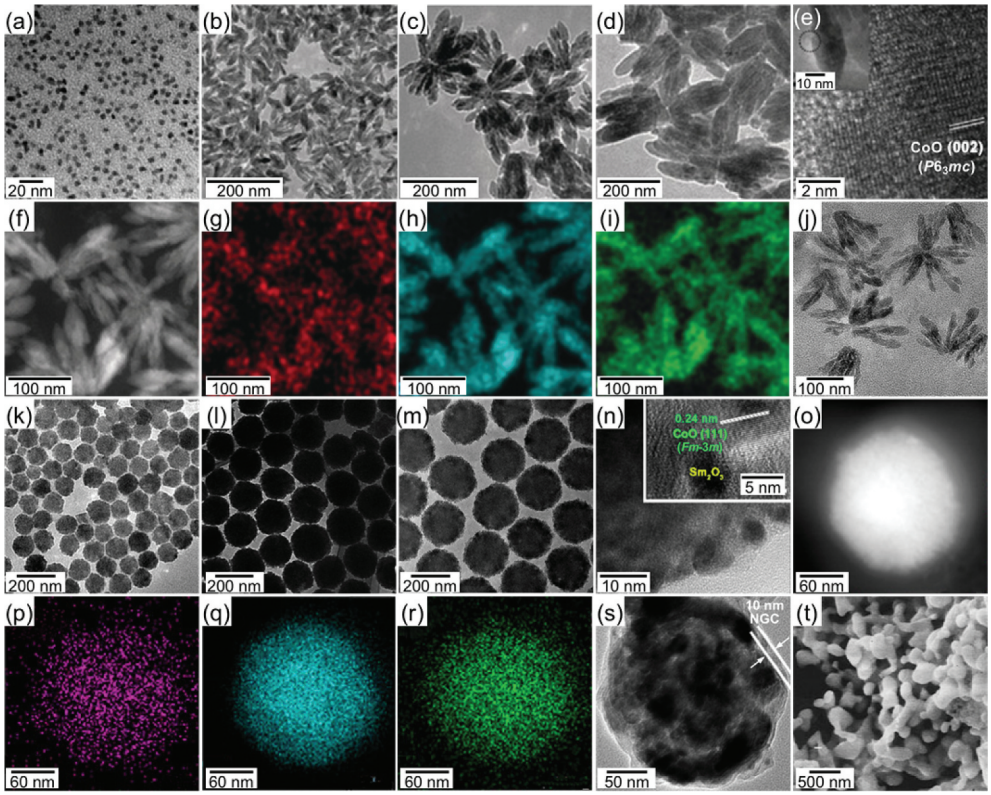

Figure 6. Chemically-synthesized nanostructured precursors. (a) TEM image of Sm–O encapsulated CoO (*Fm*-3*m*) NPs (7 nm, Sm:Co = 1:3.6). (b–d) TEM images of Sm–O encapsulated CoO ($P6_3mc$) multipods (Sm:Co = 1:4.5): (b) 60 ±10 ×10 ±3 nm, (c) 110 ±20 ×25 ±5 nm, and 220 ±40 ×45 ±5 nm. (e) HRTEM (high-resolution TEM) image of an enlarged part of a nanorod (inserted). (f) HAADF-STEM (high-angle annular dark-field scanning TEM) image and (g–i) elemental mapping images of Sm (g), Co (h), and O (i) of the multipods shown in (c). (j) TEM image of the multipods (shown in (c)) imbedded into a CaO matrix. (k–m) TEM images of Sm–O encapsulated CoO (*Fm*-3 *m*) NPs: (k) 110 ±8 nm, (l) 150 ±12 nm, (m) and 200 ±15 nm. (n) HRTEM image of a section of one 200 nm NP shown in (m), showing a mixture of smaller CoO and Sm–O NPs. (o) HAADF-STEM image and (p–r) elemental mapping images of Sm (p), Co (q), and O (r) of one representative 200 nm NP shown in (m). (s) TEM image of one 200 nm NP (shown in (m)) coated with a 10 nm layer of NGC (N-doped graphitic carbon). (t) SEM image of Fe_2O_3, $NdFeO_3$, and $Fe_2(MoO_4)_3$ mixed NPs (*ca*. 200 nm). (a) Reproduced with permission from [73]. Copyright 2020 The Royal Society of Chemistry. (b–j) Reprinted with permission from [74]. Copyright 2020 Wiley VCH. (k–t) Reproduced with permission from [75,98]. Copyright 2020 American Chemical Society.

varied below 20 at.% are suitable for the synthesis of RT_{12} MMPs.

The most simple and robust strategy for the control over the composition of the multielement R–T MMPs is to prepare mixed NPs of R–O and T–O (namely [T–O,R–O] NPs hereinafter): the precursors are synthesized *via* one-pot solution chemical synthesis; their stoichiometry is well determined by the feeding ratio of starting materials. Mixtures of Sm_2O_3/$Sm(OH)_3$, Co/Co–O/$Co(OH)_2$/CoOOH, and/or Fe/Fe–O NPs were usually prepared by reductive thermal decomposition [87], solvothermal reaction [88], co-precipitation [89–96], and ultrasonication [97]. The sol-gel method is rather simple and efficiently produces a mixture of superfine oxide NPs, where a mixture of R–O and T–O gel is formed by using a poly-network gel process at elevated temperatures, followed by calcination to convert the gel to the superfine oxides [98–100]. By varying the concentration of the R and T ions in the gel, the size of oxide NPs could be controlled in a wide range from *ca.* 10 nm to several hundred nanometers, as shown in Figure 6(t) [98]. Monodisperse and size-tunable T/T–O@R–O and RT–O nanostructured precursors with homogeneous composition have opened horizons for optimization of the microstructure of R–T MMPs since they could be embedded in dispersant matrixes (e.g., CaO, graphite oxide GO), as shown in Figure 6(j) [74,78,79], or tightly coated with other layers intact (e.g., CaO, GO, nitrogen-doped graphitic carbon NGC) in core@shell structures, as shown in Figure 6(s) [73,75,76]. While mixed NPs strategy partially succeeded in only the embedding, leading to the limited kinetic control of the microstructure of R–T MMPs [88–92,100]. Although the mixed NPs exhibited poor control of particle size, they were capable to synthesize multielement R–T MMPs owing to feasible control of composition [98].

3. Synthesis of multielement R–T MMPs

Multielement R–T intermetallics, represented by $Sm_2Fe_{17}N_3$, $(Nd,Zr)(Fe,Co,Ti)_{12}N$, and $(Sm,Zr)(Fe,Co,Ti)_{12}$, with large H_a, large M_s, and high T_c are the most promising candidates to replace $Nd_2Fe_{14}B$ for modern permanent magnet applications (Figure 1). However, their chemical synthesis remains a great challenge due to the high negative reduction potentials of R cations (e.g., Sm^{3+}: – 2.304 V, Nd^{3+}: – 2.323 V) and very low chemical stability of R metals. Generally, the R and T cations are reduced by strong reducing agents (e.g., CaH_2, Ca) accompanied by diffusion of R and T atoms to form R–T intermetallics under high-temperature solid-state reaction conditions, which is known as R–D process. Before the R–D process, it may need to remove organics from nanostructured precursors by calcination to avoid any undesirable formation of carbides and/or C interstitial compounds in the following R–D reaction, and/or adopt H_2 pre-reduction of the calcined precursors to promote the R–D reaction. In this synthesis, the R–T MMPs encounter common issues of sintering in the R–D reactions at high temperatures and oxidation in air environments. A great strategy is the coating of nanostructured precursors with stable materials, which were mentioned in Section 2, to stabilize MMPs formed in high-temperature solid-state reaction conditions and against oxidation in air. The chemical synthetic approach has been successful to prepare rather simple binary R–T MMPs. Indeed, the $SmCo_5$ and Sm_2Co_{17} MMPs with tunable sizes in a wide range from a few nanometers to a few micrometers have been successfully synthesized [65,66,73–78,80,81,87–93,97,99,100]. The resultant MMPs were dispersible in common solvents [74,75,91,100], possessed ultra-large H_c reaching the highest yet reported room-temperature $\mu_0 H_c$ of 7.2 T [91] for any permanent magnetic materials, and were strongly stable against oxidation at elevated temperatures [75]. The chemical synthesis of $SmCo_5$ MMPs has been well documented in a previous review [63]. Thus, the nanostructured precursors are readily prepared by a wide range of solution chemical synthetic methods and the intriguing results of chemically-synthesized $SmCo_5$ MMPs are triggering the chemical synthesis of MMPs of $Sm_2Fe_{17}N$ and $(R,Zr)(Fe,Co,M)_{12}$ (R = Nd, Sm; M = Ti, V, Cr, Mn, Co, Mo, W, Al, Si, Ga) compounds. The chemically synthesized MMPs of these compounds and their room-temperature magnetic properties are summarized in Table 1.

3.1. $Sm_2Fe_{17}N$ MMPs

The Sm_2Fe_{17} (Th_2Zn_{17}-type, *R*-3 *m*) compound, representative to the R_2T_{17} intermetallic series, has a relatively low $\mu_0 M_s$ = 1.03 T, very low $\mu_0 H_a$ < 1 T, and very low T_c = 116°C [100–102]. The interstitial doping of the Sm_2Fe_{17} compound with nitrogen atoms forms the $Sm_2Fe_{17}N_3$ (Th_2Zn_{17}-type, *R*-3 *m*) compound [19,101–103]; its intrinsic magnetic properties enormously increases to $\mu_0 M_s$ = 1.57 T, $\mu_0 H_a$ = 26 T, and T_c = 473°C [19], superior to those of the $Nd_2Fe_{14}B$ compound (Figure 1). Nitrogen atoms interstitially doped in the 9*e* octahedral sites (Figure 7) expand the unit-cell volume and increase the Fe–Fe exchange interactions, resulting in the increases in M_s and T_c, respectively [102–104]. The hybridization of Sm-*f* states and N-*p* states changes magnetization direction from the easy-plane in the Sm_2Fe_{17} to the easy-*c* axis in the $Sm_2Fe_{17}N_3$ and affects band energy, leading to a large uniaxial magnetocrystalline anisotropy [104]. The $Sm_2Fe_{17}N_3$ phase is metastable and, thus synthesized by nitridation of the Sm_2Fe_{17} with N_2 or NH_3 in gas-solid reaction or with melamine ($C_3H_6N_6$)

Table 1. Synthetic details and room-temperature magnetic properties of $Sm_2Fe_{17}N$ and $(R,Zr)(Fe,Co,M)_{12}$ (R = Nd, Sm; M = Ti, V, Cr, Mn, Co, Mo, W, Al, Si, Ga) MMPs synthesized by a reduction–diffusion (R–D) process. ①T/T–O@R–O NPs: core@shell structure, RT–O NPs: encapsulation, and [T–O,R–O] NPs: mixture of oxide NPs. ②Gas-solid nitridation. *High pressure. ③Solid-state nitridation. ④Dehydrogenation after the rinse with H_2O. ⑤Slow-oxidation of Ca residue before the rinse with H_2O. A typical chemically-synthetic procedure for the synthesis of multielement R–T MMPs composed of calcination, pre-reduction by H_2, and (R–D) process using Ca or CaH_2 as reductant.

	Nanostructured precursors											
Materials	Structural fashion①	Size (nm)	Calcination temperature (°C)	H_2 reduction temperature (°C)	R–D reaction (Nitridation) temperature (°C)	MMPs Size (μm)	T_c(°C)	M_s(emu g^{-1})	μ_0H_a(T)	M_r(emu g^{-1})	μ_0H_c(T)	Ref.
R_2Fe_{17} (Th_2Zn_{17}, *R*-3 *m*)												
$Sm_2Fe_{17}N$	[Fe_2O_3,Fe_3O_4,$SmFeO_3$]	*ca.* 100	500	700	900(430②)	0.7 ±0.0	–	–	–	–	2.32	[39]
		–	800	900	900(430②)	1.9 ±0.8	–	–	–	–	*ca.* 1.8	
		–	1000	900	1000(430②)	3.5 ±1.3	–	–	–	–	*ca.* 1.3	
	Fe_3O_4@Sm–O NPs	*ca.* 30	1000	900	900(435③)	1.9 ±1.0	–	–	–	–	1.3	[72]
	SmFe–O NPs	110 ±20	185	N/A	850(600②)	0.10 ±0.02	–	127.9	–	–	1.54	[74]
	[Fe–O,Sm–O] NPs	–	N/A	800	900(420②)	0.47 ±0.09	–	132	–	89	2.47④	[95]
				700	900(420②)	0.6 ±0.2	–	134	–	100	2.28④	
					950(420②)	0.9 ±0.3	–	142	–	110	1.81④	
				600	900(420②)	0.6	–	–	–	–	2.78⑤	[96]
					950(420②)	0.9	–	–	–	–	2.37⑤	
					980(420②)	1.5	–	–	–	–	2.01⑤	
RFe_{12} ($ThMn_{12}$, *I*4/*mmm*)												
$NdFe_{10}Mo_2$	[Fe_2O_3,$NdFeO_3$,$Fe_2(MoO_4)_3$]	*ca.* 200	500	700	1010	3–8	–	–	–	–	–	[98]
$NdFe_{10}Mo_2N$	[Fe_2O_3,$NdFeO_3$,$Fe_2(MoO_4)_3$]	*ca.* 200	500	700	1010 (550–600②*)	3–8	360	–	–	–	0.35	[131]
$NdFe_{10}Mo_2$	[Fe_2O_3,Nd_2O_3,MoO_3,TiO_2]	–	500	700–800	1100 (550–600②*)	–	453	65	–	–	–	[135,136]
$NdFe_{10}Mo_2H_x$							478	91	–	–	–	
$NdFe_{10}Mo_2N_x$							553	92	7.2	–	–	
$NdFe_{10.25}Mo_{1.5}Ti_{0.25}$							483	89	0.04	–	–	
$NdFe_{10.25}Mo_{1.5}Ti_{0.25}H_x$							488	93	0.04	–	–	
$NdFe_{10.25}Mo_{1.5}Ti_{0.25}N_x$							573	103	8.2	–	–	
$NdFe_{10.5}MoTi_{0.5}$							498	109	1.1	–	–	
$NdFe_{10.5}MoTi_{0.5}H_x$							508	114	1.1	–	–	
$NdFe_{10.5}MoTi_{0.5}N_x$							608	118	–	–	–	
$NdFe_{10.75}Mo_{0.5}Ti_{0.75}$							523	122	1.4	–	–	
$NdFe_{10.75}Mo_{0.5}Ti_{0.75}H_x$							533	125	1.4	–	–	
$NdFe_{10.75}Mo_{0.5}Ti_{0.75}N_x$							673	130	–	–	–	
$NdFe_{11}Ti$							533	124	1.6	–	–	
$NdFe_{11}TiH_x$							563	129	2.2	–	–	
$NdFe_{11}TiN_x$							693	127	8.0	–	–	

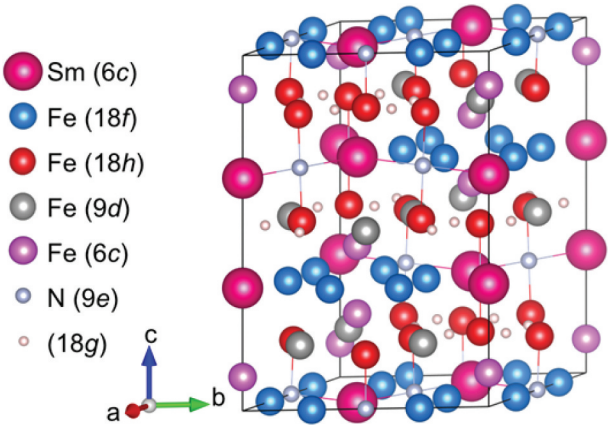

Figure 7. Crystal structure of $Sm_2Fe_{17}N_3$ (Th_2Zn_{17}, *R*-3*m*) compound.

in a solid-state reaction under high temperature and/or pressure conditions. In practice [72], the Fe_3O_4@Sm–O NPs (*ca*. 30 nm) described in Section 2 (Figure 5(b)) were calcined at 1000°C for 1 h in air (Figure 8(a,b,g(i))), and subsequently reduced by H_2 at 900°C for 1 h (Figure 8(c, d,g(ii))). The resultant NPs were converted into Sm_2Fe_{17} MMPs by the Ca R–D reaction at 900°C for 1 h in Ar, subsequently converted into $Sm_2Fe_{17}N_3$ MMPs by *in situ* nitridation at various temperatures for 10 h in N_2 (Figure 8(e,f,g(iii))). The H_c of $Sm_2Fe_{17}N_3$ MMPs depended on the nitriding temperature, as shown in Figure 8. This is related to thermal transformations in the nitridation process: nitridation in a gas-solid reaction can only proceed at relatively high temperatures (400–500°C); nitrogen concentration in $Sm_2Fe_{17}N_x$ ($0 < x \leq 3$) is a function of nitriding temperature at low temperatures, while the $Sm_2Fe_{17}N_3$ decomposed into SmN_x and Fe at high temperatures [19,105,106]. For example, the resultant $Sm_2Fe_{17}N_3$ MMPs formed by the nitridation at 435°C have an average particle size of 1.9 ±1.0 μm and a room-temperature $\mu_0 H_c$ of 1.3 T in an isotropic sample before the rinse with H_2O, as shown in Figures 8(e,f,g(iii)) and 9.

In the light of nanostructured precursors, the particle size of $Sm_2Fe_{17}N_3$ MMPs can be controlled

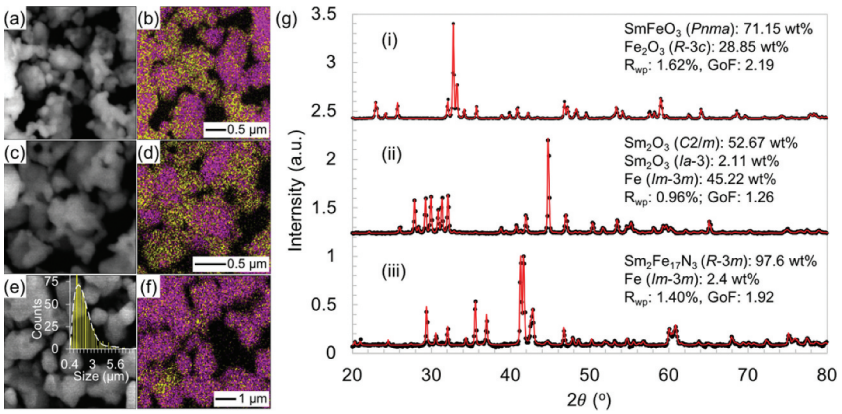

Figure 8. Structural analysis of chemically synthesized $Sm_2Fe_{17}N_3$ MMPs (*R*-3*m*, 1.9 ±1.0 μm). (a,c,e) SEM images, (b,d,f) energy-dispersive spectroscopy elemental maps (Fe K edge: purple, Sm L edge: yellow), and (g) Rietveld refinement XRD patterns of Fe_3O_4 @Sm–O NPs calcined at 1000°C for 1 h (a,b,g(i)), subsequently reduced by H_2 at 900°C for 1 h (c,d,g(ii)), and $Sm_2Fe_{17}N_3$ MMPs synthesized by Ca R–D at 900°C for 1 h in Ar and *in situ* nitridation at 435 °C for 10 h in N_2 (e,f,g(iii)). Inset in (e) shows the grain size distribution of the $Sm_2Fe_{17}N_3$ MMPs. Reproduced with permission from [72]. Copyright 2020 the Chemical Society of Japan.

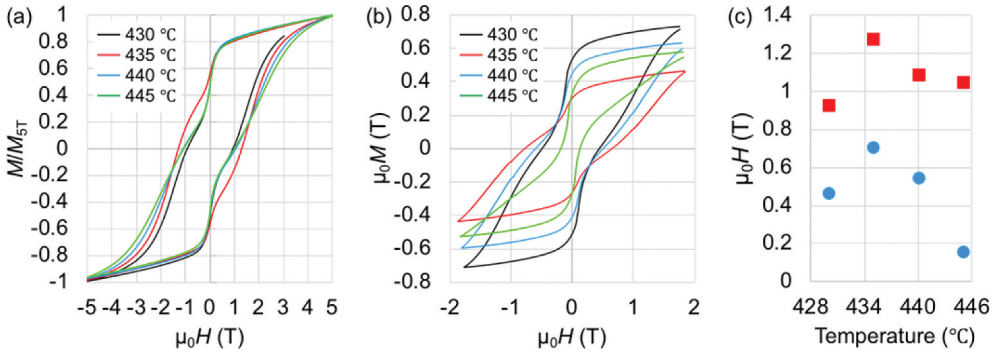

Figure 9. Room-temperature magnetic properties of $Sm_2Fe_{17}N_3$ MMPs (*R*-3 *m*, 1.9 ±1.0 μm) formed by *in situ* nitridation of Sm_2Fe_{17} MMPs at various temperatures for 10 h. (a,b) M-H curves before (a) and after (b) the rinse with H_2O. (c) Nitriding-temperature dependence of coercivity (red rectangles: before the rise with H_2O, blue circles: after the rinse with H_2O). Replotted with permission from [72]. Copyright 2020 the Chemical Society of Japan.

through thermodynamics based on careful observation of reaction temperature [39]. To this end, a synthesis using a mixture of Fe–O and Sm–O NPs prepared by a sol-gel method, as described in Section 2, was conducted *via* consecutive calcination, H_2 pre-reduction, and Ca R–D at various temperatures in the ranges of 500–1000°C, 700–900°C, and 900–1000°C, respectively, followed by *in situ* nitridation at 430 °C. The particle size of the resultant $Sm_2Fe_{17}N_3$ MMPs was largely dependent on the processing temperature. The first two processes conducted at low temperatures were crucially important to control the final MMP size at the following R–D process as their resultant small NPs facilitated the Ca R–D reaction at low temperatures to obtain small MMPs. The Ca R–D process, in its turn, effectively determined the particle size of the resultant $Sm_2Fe_{17}N_3$ MMPs as higher R–D reaction temperatures led to larger MMPs due to the sintering of the particles. As a result, the $Sm_2Fe_{17}N_3$ MMPs exhibited particle sizes tuned in the range of 0.7–3.5 μm and room-temperature μ_0H_c tuned in the range of 1.3–2.32 T in anisotropic samples. The smallest size of 0.69 μm was obtained at the lowest temperatures for the calcination at 500°C, H_2 pre-reduction at 700°C, and Ca R–D processes at 900°C. The H_c showed an obvious manifestation of size dependence and its highest μ_0H_c of 2.32 T was obtained for the smallest size of 0.69 μm (Figure 2(a), the blue rectangles). However, the syntheses above required an excessive amount of Sm by 25–30 at.% to the 2:17 stoichiometry to compensate for Sm evaporation during the Ca R–D reaction. The thermodynamic control could not proceed to obtain much smaller sizes as the calciothermic reduction must be conducted at temperatures far above the melting point of Ca (845°C). Recently, an efficient kinetic approach that was advanced by the engineering of nanostructured precursors could achieve the formation of $Sm_2Fe_{17}N_3$ MMPs with better-controlled size and composition by Sun and co-workers [74]. In this synthesis, SmFe–O nanocubes (110 nm) were tightly coated with CaO by thermal decomposition of $Ca(acac)_2$ at 200°C, calcined at 185°C for 5 h, and reduced by Ca at 850°C for 30 min in Ar. The resultant Sm_2Fe_{17} MMPs were then mixed with $C_3H_6N_6$ and annealed at 600°C for 6 h in Ar to form 100 nm $Sm_2Fe_{17}N_3$ MMPs. The overall synthesis costed an excessive Sm composition of the SmFe–O nanocubes by only 2 at.% to the 2:17 stoichiometry to compensate for Sm loss. The resultant $Sm_2Fe_{17}N_3$ MMPs were well dispersible in conventional solvents and exhibited room-temperature μ_0H_c of 1.54 T in an anisotropic PEG–embedded $Sm_2Fe_{17}N_3$ (PEG = polyethylene glycol) sample. This H_c value was smaller than that reported above because their particle size (100 nm) was smaller than the single-domain critical diameter of $Sm_2Fe_{17}N_3$, D_{sd} = *ca.* 390 nm [36]. This method would give the $Sm_2Fe_{17}N_3$ MMPs with larger sizes approaching the D_{sd} by increasing the particle size of the precursors, leading to ultra-large H_c.

3.2. RT_{12} MMPs

$NdFe_{12}N$ ($ThMn_{12}$-type, *I*4/*mmm*) and $Sm(Fe,Co)_{12}$ ($ThMn_{12}$-type, *I*4/*mmm*) compounds are the most impressive candidates for rare-earth-element-lean permanent magnets: their thin films were found to possess significantly large M_s and H_a (Figure 1), $(BH)_{max}$ theoretical limits of 550 and 630 kJm^{-3}, respectively, and high T_c of 550 and 586°C, respectively; all the properties surpass those of the $Nd_2Fe_{14}B$ [15,20,107–109]. Recently, anisotropic $Sm(Fe_{0.8}Co_{0.2})_{12}$–B films composed of columnar grains (40 nm) textured with amorphous B intergranular boundary have been realized. The films exhibited a large room-temperature μ_0H_c of 1.2 T, μ_0M_r of 1.5 T, and very small temperature-dependent H_c, promising excellent stability at $T \geq$ 150°C [110]. Unfortunately, they are metastable phases and, thus could not be realized in bulk for the fabrication of PMs. To this end, one can partially substitute Fe with stabilizing elements M (M = Ti, V, Cr, Mn, Co, Mo, W, Al, Si, Ga) in preferential 8*f*, 8*i*, and 8*j* sites, depending on the stabilizing elements, for example, Ti, V, and Mo in 8*i*; Co and Si in 8 *f* and 8 *j*; Ga in 8 *j*, as shown inFigure 10 [12,13,17,18,40–50,106,111–117]. The substitution with a large concentration of M leads to a significant reduction in M_s, except for Co, as shown in Figure 1 for Ti. The Co substitution results in the M_s enhancement based on the Slater-Pauling curve, which is elucidated by an increase in the majority-spin state density below the Fermi level [114,117]. An effective strategy that stabilizes the low M-substituted concentration compounds and rationally enhances M_s is to substitute Sm or Nd with other R elements of smaller atomic number (e.g., Zr, Y) in preferential 2*a* sites (Figure 10), though it reduces H_a for Zr, as shown in Figure 1 [16,21,22,117–126]. The substituted compounds have been found to be stable at even very high temperatures [127]. The stabilization by the substitution can be understood as a decrease of local mismatches in interatomic distances in the structure unfavorable for the orbital hybridization [121],

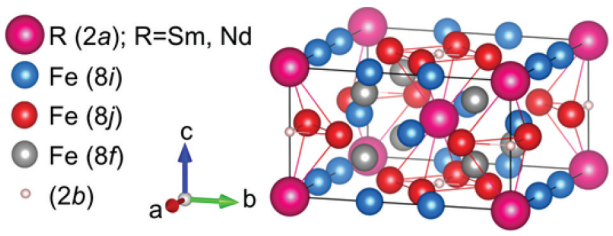

Figure 10. Crystal structure of RFe_{12} ($ThMn_{12}$, *I*4/*mmm*) compounds (R = Sm, Nd).

resulting in low formation energies of the substituted compounds [114,126]. Interstitial nitrogen doping into 2*b* octahedral sites in $Nd(Fe,M)_{12}$ (Figure 10) is of crucial importance to enhance M_s and H_a; it could be explained as the hybridization between N-*p* (2*b*) and Fe-*d* (8*j*) gives raises in the magnetic moment and the crystal field parameter $r^2A_2^0$ [128,129].

Despite such impressive H_a and enormous research efforts, the RT_{12} MMPs with substantial H_c have not been realized yet, the reported H_c values being still less than 10% of the corresponding H_a [40–50,111,112,124]. The following critical issues make it extremely difficult to practically realize the hard magnetic potential of RT_{12} compounds. Firstly, the size and shape of RT_{12} MMPs have not been well optimized, especially in the sub-micrometer range, as shown in Figure 2(b) [40–50,111,112,124]. Secondly, since equilibrium phases formed along with the typical RT_{12} phase are ferromagnetic, the conventional methods cannot introduce appropriate non-magnetic intergranular boundary phases, unlike $Nd_2Fe_{14}B$ where their intergranular boundary is greatly facilitated by the eutectic reaction with Nd phase [8,21,111,130]. Finally, the RT_{12} compounds usually melt at relatively high temperatures, making it difficult to fabricate anisotropic magnets through the liquid-phase sintering [8,21,111,130]. Chemically synthesized fine RT_{12} MMPs with optimum microstructure may become suitable for sintering into fully dense anisotropic magnets, but is greatly challenging to be obtained. In a typical synthesis, a mixture of Fe_2O_3 ($P4_12_12$, *R*-3*c*), $NdFeO_3$ (*Pnma*), and $Fe_2(MoO_4)_3$ ($P2_1/c$, *Pbcn*) NPs (*ca.* 200 nm), as described in Section 2 (Figure 6(t)), reduced by H_2 at 700°C to convert into Fe(Mo) alloyed (*Im*-3*m*) and Nd_2O_3 (*C*2/*m*, *P*-3*m*1) NPs, and subsequently converted into $NdFe_{10}Mo_2$ (*I*4/*mmm*) MMPs (*ca.* 3–8 μm) by CaH_2 R–D at 1010°C for 4 h (Figure 11(a,b)) [98]. The particle size of the oxide NPs was crucial in controlling the particle size of $NdFe_{10}Mo_2$ MMPs: the CaH_2 R–D reaction could be carried out at lower temperatures (*e.g.*, 960°C) and for a short time for the smaller oxide NPs (*ca.* 50 nm), resulting in smaller $NdFe_{10}Mo_2$ MMPs [98,131]. The nitridation of $NdFe_{11}Ti$ was conducted using the same procedure for the synthesis of $Sm_2Fe_{17}N_3$, as described in Section 3.1, but at higher temperatures (550–600°C). As a result, the $NdFe_{10}Mo_2N$ MMPs (*ca.* 3–8 μm) exhibited a room-temperature μ_0H_c of 0.35 T [131]. The method has been successfully applied to synthesize a series of ternary, quaternary, and quinary $R(Fe,M)_{12}X$ (R = Nd, Y, Nb, Tb, Er; M = Ti, Mo, W, Si; X = N, H) MMPs, as shown in Table 1 [131–136]. For the formation of the $R(Fe,M)_{12}X$ phase almost free from impurities such as Fe and/or $TiFe_2$ phases, these syntheses were required to compensate the Sm evaporation in Ca R–D process of 2–10 at.% exceeded to the 1:12 stoichiometry, depending on R elements. Since the formation of $R(Fe,M)_{12}X$ phase required very high temperature (960–1100°C) for long reaction time (4–8 h), the particle sizes of resultant MMPs were in the range of 3–8 μm. The size control through thermodynamics, which is applicable for $Sm_2Fe_{17}N_3$, is no longer effective for RT_{12} in the mesoscopic scale in such high-temperature reactions. The particle size may be further controlled to some extent through kinetics, in which the mixed oxide NPs are embedded in dispersant matrixes (e.g., CaO, GO) to suppress the resultant MMPs from sintering. A more effective

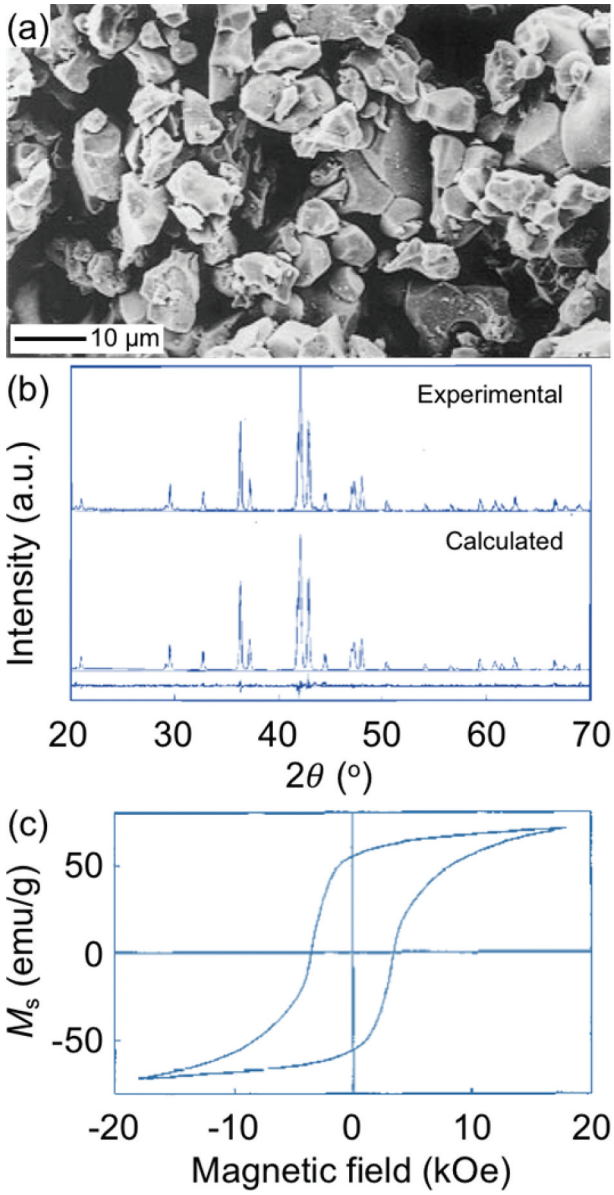

Figure 11. Structural analysis and room-temperature magnetic properties of chemically synthesized $NdFe_{10}Mo_2$ and $NdFe_{10}Mo_2N$ MMPs (*I*4/*mmm*, 3–8 μm). (a) SEM image and (b) XRD patterns of $NdFe_{10}Mo_2$ MMPs synthesized using CaH_2 R–D at 1010 °C for 4 h. (c) M-H curve of $NdFe_{10}Mo_2N$ MMPs synthesized by nitridation of $NdFe_{10}Mo_2$ MMPs, showing μ_0H_c of 0.35 T. (a,b) Reproduced with permission from [98]. Copyright 2020 American Chemical Society. (c) Reprinted with permission from [131]. Copyright 2020 Elsevier.

approach to the kinetic control is to adopt encapsulated nanostructures as precursors (Figure 6(a–s)), where all elements are incorporated in a single NPs with homogeneous composition. We have examined the feasibility of this approach for the synthesis of quinary (Sm,Zr)(Fe,Co,Ti)$_{12}$ MMPs using Sm–O, Zr–O, and Ti–O encapsulated $CoFe_2O_4$ (*Fd*-3*m*) NPs (5 nm), which was mentioned in Section 2. As a result, we have successfully synthesized ultrafine (Sm,Zr)(Fe,Co,Ti)$_{12}$ MMPs with partially controllable size. The resulting (Sm,Zr)(Fe,Co,Ti)$_{12}$ MMPs exhibited a relatively large room-temperature H_c and high susceptibility to magnetic-field alignment, resulting in anisotropic bulk magnets with a large $(BH)_{max}$, which will be reported in the forthcoming paper. Taking these potentials into consideration, synthetic prospects will move a step forward in the size control through kinetics, which is advanced by the use of encapsulated nanostructure as precursors, to obtain their particle size in the range below 1 μm.

3.3. Oxidation and Hydrogenation of R–T MMPs

The chemical synthesis of R–T MMPs involves calciothermic reduction, resulting in the formation of byproducts (e.g., CaO, $CaCO_3$) and residual reductants (e.g., CaH_2 or Ca). Therefore, a post purifying process is required; however, it is still a challenge to achieve high purity and improved magnetic properties of R–T MMPs. The purification using water-based solutions as a rinsing agent has been found to form side products and, thus affect the magnetic properties of as-synthesized R–T MMPs to some extent [81]. Generally, water-rinsing induced oxidation and hydrogenation of R–T MMPs are inevitable side reactions. Owing to low ionization potentials, R elements can be easily oxidized to form surface oxides once R–T MMPs are exposed to air environment, especially in acidic solutions, leading to an attenuation of magnetic performance. Recently, a new washing process has been reported for highly effective purification and stabilization against oxidation of Sm–Co and $Nd_2Fe_{14}B$ MMPs by Choa and co-workers [81]. In this procedure, a methanol solution of NH_4Cl was used as a rinsing agent, in which Ca and CaO react with NH_4Cl to form NH_3 and methanol-soluble $CaCl_2$. As a result, neither surface oxidation nor any damage to the MMPs was observed by HRTEM characterization, resulting in a substantial improvement of M_s, even near a M_s theoretical value for Sm–Co MMPs. For the nanoscale R–T MMPs sensitive to air, the situation is much severe at elevated temperatures. Their protection against long-term and severe oxidation is crucially important for practical applications, especially for high-temperature applications. Recently, Sun et al. demonstrated a new strategy for the chemical synthesis and stabilization of $SmCo_5$ NPs for high-performance upnanomagnet applications in a broad temperature range [75]. In particular, the chemically synthesized SmCo–O NPs composed of Sm_2O_3 and CoO were coated with a layer of NGC (Figure 6(s)), embedded in CaO matrix, and reduced by Ca at 850°C to produce $SmCo_5$@NGC MMPs. The resultant $SmCo_5$@NGC MMPs showed efficient stability against oxidation: they could maintain 99.2% or 98.3% of magnetization after their exposure to air at room temperature for 5 days or 100°C for 48 h, respectively. The protection of R–T MMPs against oxidation is also necessary to prevent the oxidation induced decomposition. It has been found that the $(Sm_{0.8}Zr_{0.2})(Fe_{0.75}Co_{0.25})_{11.5}Ti_{0.5}$ phase was stable at very high temperatures up to at least 1100°C in an almost oxygen-free atmosphere, but was decomposed above 427°C [127].down

Hydrogenation of R–T MMPs through the exothermic reaction of residual Ca with H_2O in a rinsing process using water-based solutions has been found to considerably reduce H_c of $Sm_2Fe_{17}N_3$ MMPs [72,95,96]. As seen in Figure 9, the H_c of $Sm_2Fe_{17}N_3$ MMPs rinsed with distilled H_2O is reduced by 40–80% those of as-synthesized ones. This could be understood as H atoms interstitially occupy available 18*g* tetrahedral sites (Figure 7) to cause a decrease in H_a [137,138]. It was also obviously observed that the dehydrogenation of hydrogen-doped $Sm_2Fe_{17}N_3$ MMPs by means of annealing in vacuum was ineffective to recover their H_c [95]. As a result, the $Sm_2Fe_{17}N_3$ MMPs (0.6 μm) exhibited room-temperature $\mu_0 H_c$ of 2.8 T, 1.56 T, and 2.28 T in the form of anisotropic samples for as-synthesis, rinse with distilled water, and a combination of the rinse and dehydrogenation in a reduced atmosphere at 200°C, respectively. Slow oxidation of residual Ca to CaO, prior to the rising process, was then applied to avoid the *in situ* formation of H_2, resulting in the H_c preservation of as-synthesized $Sm_2Fe_{17}N_3$ MMPs [96]. However, the oxidation also generated water-insoluble Sm_2O_3 and $CaCO_3$ impurities, deteriorating M_s. The purification process using a NH_4Cl/methanol solution, as previously described [81], is greatly capable of selectively rinsing out impurities and avoiding the *in situ* generation H_2; it has been extended to successfully prepare dispersible $Sm_2Fe_{17}N_3$ MMP [74]. Unlike what was observed in the $Sm_2Fe_{17}N_3$ compound, hydrogen interstitial doping in preferential 2*b* octahedral sites in RT_{12} compound (Figure 10) has been found to enhance their M_s, H_a, and T_c [132–135,139–147]. The increase in H_a was attributed to an increase in the crystal field and a change in the local symmetry of 4*f*-electron shell along the *c*-axis, while the increases in M_s and T_c were attributed to an unit-cell-volume expansion and strong Fe–Fe exchange interactions, respectively, beyond the hydrogen interstitial doping [139–147].

4. R–T/T exchange-coupled NCMs

Magnetically hard/soft exchange-coupled NCMs have long been a potential candidate for high-performance permanent magnets since it can possess a large $(BH)_{max}$, which is deduced from large H_a and M_s of the corresponding hard and soft magnetic constituents, respectively [148,149]. Subject to the R elements crisis, they have the high potential to meet current demands for R-element-lean PMs with large $(BH)_{max}$ and operating temperatures of 150–200°C. The effectiveness of exchange-coupled interaction, which is represented by the microstructure factor α [25–29], is inversely proportional to the ratio D_s/δ_w, where D_s is the size of a soft magnetic phase and $\delta_w = \pi\sqrt{A_{ex}/K_1}$ is the domain wall width of a hard magnetic phase [148,149]. An effective exchange-coupled interaction requires the size of the soft magnetic phase being small enough ($D_s < 2\delta_w$ for anisotropic bulk NCMs) and the size of the hard magnetic phase approaching the exchange length (l_{ex}) of the soft magnetic phase [148–151]. These fundamentals have led to two following approaches to the development in the exchange-coupled NCMs based on the hard magnetic materials. One is to adopt materials with a large K_1 but a consequently small δ_w, such as $L1_0$-FePt [152], $Nd_2Fe_{14}B$ [153,154], $SmCo_5$ [87,155–158], and $Sm_2Fe_{17}N_3$ [150], as their large H_a compensated for a small M_s corresponding to a small D_s (D_s < *ca.* 10 nm) [148,149]. Another is to adopt materials with a moderate K_1 and a consequently relatively large δ_w, such as $L1_0$-FePd [159–161] and $HfCo_7$ [162], as they had benefitted to α and D_s, and a large M_s corresponding to a large D_s (D_s < *ca.* 20 nm) could be compensated for a moderate H_a [148,149,161,162]. The latter approach is not usually considered, since the gain in α is overcompensated by the reduction of H_a.

Apart from the microstructure issues above, the most obvious obstacle to the synthesis of R–T/T NCMs is the formation of undesirable phases as the R and T metals can form many equilibrium and metastable phases. The design of magnetically hard/soft exchange-coupled NCMs with the soft phase as an equilibrium phase of the hard phase, which is similar to the one that was proved to be so effective in $L1_0$-FePd/Fe NCMs [159–161], is a solution. Chemical synthesis of R–T/T NCMs has had very limited success in obtaining large $(BH)_{max}$. The $Sm_2Fe_{17}N_3$ has a large K_1 of 16.2 MJm^{-3} [19]; the $Sm_2Fe_{17}N_3$ (2.4 nm)/$Fe_{65}Co_{35}$ (9 nm) alternatively multilayered anisotropic NCMs have been theoretically predicted to have a grant $(BH)_{max}$ of 1 MJm^{-3} (120 MG Oe) [149]. Nevertheless, large $(BH)_{max}$ of $Sm_2Fe_{17}N_3$ NCMs has never been realized, because there has still no their bulk materials prepared with a grain size of the order of 10 nm, where large H_c and M_r could be achieved in their NCMs [150,151]. Since this size range is an unrealistic practice for metastable $Sm_2Fe_{17}N_3$, little attention has been paid to the $Sm_2Fe_{17}N_3$ NCMs so far. Owing to it's a huge K_1 of 17.2 MJm^{-3}, a relatively small $\mu_0 M_s$ of 1.07 T [36], and easy chemical synthesis among R–T intermetallics, the $SmCo_5$ has drawn considerable attention as a hard magnetic phase [87,155–158]. Generally, the $SmCo_5$/Fe NCMs were synthesized by a simultaneous Ca R–D of mixed oxide NPs [87,155,156]; they exhibited very small M_r, resulting in very small $(BH)_{max}$. The main reason for such the reported small $(BH)_{max}$ in the $SmCo_5$/Fe NCMs is a lack of an easy-axis alignment of the hard magnetic $SmCo_5$ phase. It has been demonstrated that the anisotropic FePt/$Fe_{0.8}Ni_{0.2}$ NCMs could enhance $(BH)_{max}$ by 224% of that of the corresponding isotropic NCMs [163]. Therefore, chemical synthesis of particulate NCMs, which is similar to the ones that were proved to be so effective in $L1_0$-FePd/Fe NCMs [161] and $HfCo_7/Fe_{65}Co_{35}$ NCMs [162], is of crucial importance to fabricate the anisotropic NCMs with ultra-large $(BH)_{max}$. In a typical synthesis [157], particulate $SmCo_5$/Co MMPs (200 nm, Co-soft phase: 4 wt.%) were synthesized by Ca R–D of $Sm[Co(CN)_6]\cdot 4H_2O$@GO MMPs and $Co(acac)_2$ additive at 960°C; their isotropic sample showed room-temperature $\mu_0 H_c$ of 2.07 T, M_r/M_s of 0.75, and $(BH)_{max}$ of 80 kJm^{-3} (10 MG Oe). This small $(BH)_{max}$ resulted from a low fraction of the soft magnetic Co phase (4 wt.%) and/or too large grain size of the hard magnetic $SmCo_5$ phase (*ca.* 200 nm) to an effective exchange coupling [148–151]. It is highly perspective to gain a drastically enhanced $(BH)_{max}$ as the particulate $SmCo_5$/Co MMPs can be magnetically aligned to form the anisotropic NCMs. In the line with the problem of R–T/T NCMs, the great challenge in the synthesis of $SmCo_5$/Fe(or Co) NCMs is to achieve a high fraction of the soft phase since other phases can be formed with the increase in the fraction [155,157]. An effective chemical synthesis avoiding this alloying issue is to disperse SiO_2-coated Fe NPs in $SmCo_5$ matrix, which is described in the literature elsewhere [156]. Prospects are presumably better for RT_{12}/T NCMs, where T is the only equilibrium phase of the RT_{12} phase at their high fraction. There have unfortunately been no reports on the RT_{12}/T NCMs yet.

5. Conclusions and prospects

Multicomponent R–T permanent magnetic materials, which are multielement or multi-phase ones, are expected to shape the growth of $(BH)_{max}$ back to the 'Moore's law' after decades of $Nd_2Fe_{14}B$ magnets since the theoretical $(BH)_{max}$ limit is given by $\mu_0 M_s^2/4$ while the M_s can further increase (Figure 1). However, extraordinary achievements in searching for high-

performance magnetic materials with ultra-large intrinsic properties with the aid of theoretical calculations in recent years, especially $(R,Zr)(Fe,Co,Ti)_{12}$ (R = Nd, Sm) compounds (Figure 1), leave a large gap behind them to the fabrication of their corresponding magnets. This lag practically comes from challenges in the synthesis of these compounds with optimum microstructure in the mesoscopic range for maximizing practically relevant extrinsic properties and the introduction of appropriate grain boundaries for the fabrication of their anisotropic magnets. While conventional synthetic techniques that are popular with the production of magnetic material powders remain unsatisfactory, chemical synthetic approach with recent advances in the solution-phase synthesis of nanostructured precursors followed by solid-state reaction may become suitable to overcome the challenges. As nanostructured precursors are used, the chemical approach broadens microstructural control horizons given by thermodynamics and kinetics. The thermodynamics, unfortunately, addresses a limit in the size control of RT_{12} intermetallics, where their formation requires very high temperatures. Prospects seem to be only adopting the kinetic control, where appropriate engineering of nanostructured precursors toward the following solid-state reaction is a crucial key. The ideal nanostructured precursors are particulate NPs composed of all constituents, and they are monodisperse and homogenous in composition. In addition to the precedent challenges in the synthesis of R–T intermetallics, the synthesis of R–T/T NCMs faces new problems of achieving the R–T phase with a particle size of the order of 10 nm for effective exchange interactions, and the formation of undesired phases with an increase in the T fraction. As a result, while monodisperse $Sm_2Fe_{17}N_3$ MMPs with very well-controllable size and ultra-large H_c are ready for the fabrication of anisotropic magnets, progress in the development of $(R,Zr)(Fe,Co,Ti)_{12}$ MMPs and R–T/T NCMs remains marginal. Once MMPs with primarily optimum microstructure are synthesized, their anisotropic magnets can be fabricated by a rapid low-temperature current sintering method [164] or an infiltration treatment [165], instead of conventional liquid-phase sintering.

Disclosure statement

No potential conflict of interest was reported by the authors.

Funding

This work was supported by the Elements Strategy Initiative Center for Magnetic Materials (ESICMM) project (No. JPMXP0112101004) from the Ministry of Education, Culture, Sports, Science, and Technology (MEXT), Japan.

Notes on contributors

T. Thuy Trinh is a program-specific assistant professor at Kyoto University. He received his PhD in Materials Science from Japan Advanced Institute of Science and Technology in 2012. His research interest is in functional nanomaterials for energy-related applications, including but not limited to magnetic nanomaterials.

Jungryang Kim is a researcher at National Institute of Advanced Industrial Science and Technology (AIST). She received her PhD from Kyoto University. Her research interests include material science, especially material synthesis, and present main research is the permanent magnetic materials.

Ryota Sato is currently an assistant professor at Kyoto University. He received his PhD from University of Tsukuba. His research interests include the development of wet-chemical methods to synthesize monodisperse inorganic nanoparticles with precisely controlled nanostructures (size, shape, morphology, composition, etc.) and their application for magnetic, catalytic, and plasmonic nanomaterials. Nowadays, in particular, he is interested in pseudomorphic and element-selective replacement reactions of multinary inorganic nanoparticles that can provide us with novel substances and their unique properties.

Kenshi Matsumoto is a program-specific associate professor at Kyoto University. He received his PhD at Kyoto University in 2019 under the supervisor of Prof. Toshiharu Teranishi. His research interests include the formation of nanoparticles with novel crystal structure for high-performance magnetic properties.

Toshiharu Teranishi is a full-professor at Kyoto University and a specially-appointed professor at Tokyo Institute of Technology. He received his PhD from The University of Tokyo. His research interests include precise structural control of inorganic nanomaterials and structure-specific functions for high-performance devices and photo-energy conversion. He is serving as a vice president of the Society of Nano Science and Technology, Japan, and an associate member of Science Council of Japan. He is also serving as an Associate Editor of Chemical Science (RSC) and an Advisory Board of ChemNanoMat (Wiley VCH).

ORCID

T. Thuy Trinh http://orcid.org/0000-0002-5234-7810
Jungryang Kim http://orcid.org/0000-0001-5106-3296
Ryota Sato http://orcid.org/0000-0002-7353-6880
Kenshi Matsumoto http://orcid.org/0000-0002-5680-330X
Toshiharu Teranishi http://orcid.org/0000-0002-5818-8865

References

[1] Hirosawa S, Matsuura Y, Yamamoto H, et al. Magnetization and magnetic anisotropy of $R_2Fe_{14}B$ measured on single crystals. J Appl Phys. 1986;59:873–879.
[2] Sagawa M, Hirosawa S, Yamamoto H, et al. Nd–Fe–B permanent magnet materials. Jpn J Appl Phys. 1987;26:785–800.

[3] Matsuura Y. Recent development of Nd–Fe–B sintered magnets and their applications. J Magn Magn Mater. 2006;303:344–347.
[4] Gutfleisch O, Willard MA, Brück E, et al. Magnetic materials and devices for the 21st century: stronger, lighter, and more energy efficient. Adv Mater. 2011;23:821–842.
[5] Sugimoto S. Current status and recent topics of rare-earth permanent magnets. J Phys D: Appl Phys. 2011;44:064001.
[6] Hirosawa S. Current status of research and development toward permanent magnets free from critical elements. 2015;39:85–95.
[7] Hirosawa S, Nishino M, Miyashita S. Perspectives for high-performance permanent magnets: applications, coercivity, and new materials. Adv Nat Sci. 2017;8:013002.
[8] Coey JMD. Perspective and prospects for rare earth permanent magnets. Engineering. 2020;6:119–131.
[9] Miyake T, Akai H. Quantum theory of rare-earth magnets. J Phys Soc Jpn. 2018;87:041009.
[10] Akai H. Maximum performance of permanent magnet materials. Scr Mater. 2018;154:300–304.
[11] Weller D, Moser A, Folks L, et al. High Ku materials approach to 100 Gbits/in2. IEEE Trans Magn. 2000;36:10–15.
[12] Yang YC, Zhang XD, Ge SL, et al. Magnetic and crystallographic properties of novel Fe-rich rare-earth nitrides of the type RTiFe11N1-δ (invited). J Appl Phys. 1991;70:6001–6005.
[13] Akayama M, Fujii H, Yamamoto K, et al. Physical properties of nitrogenated RFe11Ti intermetallic compounds (R = Ce, Pr and Nd) with ThMn12-type structure. J Magn Magn Mater. 1994;130:99–107.
[14] Sakurada S, Tsutai A, Hirai T, et al. Structural and magnetic properties of rapidly quenched (R,Zr)(Fe,Co) 10Nx (R=Nd, Sm). J Appl Phys. 1996;79:4611–4613.
[15] Hirayama Y, Takahashi YK, Hirosawa S, et al. NdFe12Nx hard-magnetic compound with high magnetization and anisotropy field. Scr Mater. 2015;95:70–72.
[16] Suzuki S, Kuno T, Urushibata K, et al. A new magnet material with ThMn12 structure: (Nd1-xZrx) (Fe1-yCoy)11+zTi1-zNα (α = 0.6–1.3). J Magn Magn Mater. 2016;401:259–268.
[17] Ohashi K, Tawara Y, Osugi R, et al. Magnetic properties of Fe-rich rare-earth intermetallic compounds with a ThMn12 structure. J Appl Phys. 1988;64:5714–5716.
[18] Cheng SF, Sinha VK, Xu Y, et al. Magnetic and structural properties of SmTiFe11-xCox alloys. J Magn Magn Mater. 1988;75:330–338.
[19] Iriyama T, Kobayashi K, Imaoka N, et al. Effect of nitrogen content on magnetic properties of Sm2Fel7Nx (0 < x < 6). IEEE Trans Magn. 1992;28:2326–2331.
[20] Hirayama Y, Takahashi YK, Hirosawa S, et al. Intrinsic hard magnetic properties of Sm(Fe1-xCox) 12 compound with the ThMn12 structure. Scr Mater. 2017;138:62–65.
[21] Gabay MA, Hadjipanayis GC. Recent developments in RFe12-type compounds for permanent magnets. Scr Mater. 2018;154:284–288.
[22] Tozman P, Sepehri-Amin H, Takahashi YK, et al. Intrinsic magnetic properties of Sm(Fe1-xCox)11Ti and Zr–substituted Sm1-yZry(Fe0.8Co0.2)11.5Ti0.5 compounds with ThMn12 structure toward the development of permanent magnets. Acta Materialia. 2018;153:354–363.
[23] Aharoni A. Theoretical search for domain nucleation. Rev Mod Phys. 1962;34:227–238.
[24] Brown WF. Micromagnetics. New York: Wiley; 1963.
[25] Kronmüller H. Theory of nucleation fields in inhomogeneous ferromagnets. Phys Stat Sol (B). 1987; 144:385–396.
[26] Kronmüller H, Durst K-D, Sagawa M. Analysis of the magnetic hardening mechanism in RE-FeB permanent magnets. J Magn Magn Mater. 1988;74:291–302.
[27] Coey JMD. Rare-earth iron permanent magnets. Oxford: Oxford University Press; 1996.
[28] Givord D, Rossignol M, Barthem VMTS. The physics of coercivity. J Magn Magn Mater. 2003;258–259:1–5.
[29] Skomski R. Nanomagnetics. J Phys Condens Matter. 2003;15:R841–R896.
[30] Balamurugan B, Sellmyer DJ, Hadjipanayis GC, et al. Prospects for nanoparticle-based permanent magnets. Scr Mater. 2012;67:542–547.
[31] Poudyal N, Liu JP. Advances in nanostructured permanent magnets research. J Phys D: Appl Phys. 2013;46:043001.
[32] Yue M, Zhang Z, Liu JP. Fabrication of bulk nanostructured permanent magnets with high energy density: challenges and approaches. Nanoscale. 2017;9: 3674–3697.
[33] Kittel C. Theory of the structure of ferromagnetic domains in films and small particles. Phys Rev. 1945;70:965–971.
[34] Kittel C. Physical theory of ferromagnetic domains. Rev Mod Phys. 1949;21:541–583.
[35] O'Handley RC. Modern magnetic materials: principles and applications. Weinheim: Wiley-VCH; 2000.
[36] Coey JMD. Magnetism and magnetic materials. Cambridge, U.K.: Cambridge University Press; 2010.
[37] Imaoka N, Iriyama T, Itoh S, et al. Effect of Mn addition to Sm-Fe-N magnets on the thermal stability of coercivity. J Alloys Compd. 1995;222:73–77.
[38] Tada S, Tomimoto T, Kume M. REPM'12 Proc. 2012. p. 48–53.
[39] Hirayama Y, Panda AK, Ohkubo T, et al. High coercivity Sm2Fe17N3 submicron size powder prepared by polymerized-complex and reduction–diffusion process. Scr Mater. 2016;120:27–30.
[40] Stmeszewski J, Wang YZ, Singleton EW, et al. High coercivity in Sm(FeT)12 type magnets. IEEE Trans Magn. 1989;25:3309–3311.
[41] Okada M, Yamagishi K, Homma M. High coercivity in melt-spun SmFe10(TiV) ribbons. Mater Trans JIM. 1989;30:374–377.
[42] Sun H, Otani Y, Coey JMD. Coercivity and microstructure of melt-spun Sm(Fe11Ti). J Appl Phys. 1990;67:4659–4661.
[43] Wang Y, Hadjipanayis GC, Kim A, et al. Magnetic and structural studies in Sm-Fe-Ti magnets. J Appl Phys. 1990;67:4954–4956.
[44] Sugimoto S, Kojima A, Okada M, et al. Enhancement of magnetic properties of Sm(Fe,Co,Ti)12 melt-spun ribbons by refining crystalized grains. Mater Trans JIM. 1991;32:1180–1183.
[45] Suzuki S, Inoue N, Miura T. Magnetic properties of RFe11-xCoxTiNy (R: Nd, Pr) compounds with ThMn12 type structure. IEEE Tran Magn. 1992; 28:2005–2009.
[46] Bessais L, Djega-Mariadassou C. Structure and magnetic properties of nanocrystalline SmFe1-xCoxTi11 (x ≤ 2). Phys Rev B. 2001;79:054412.

[47] Gong W, Hadjipanayis GC. Nitrogenated 1:12 Compounds Prepared by Mechanical Alloying. IEEE Trans Magn. 1992;28:2563–2565.
[48] Pinkerton FE, Van Wingerden DJ. Magnetic hardening of SmFe10V2 by melt-spinning. IEEE Trans Magn. 1989;25:3306–3308.
[49] Singleton EW, Strzeszewski J, Hadjipanayis JC, et al. Magnetic and structural properties of melt-spun rare-earth transition-metal intermetallics with ThMn12 structure. J Appl Phys. 1988;64:5717–5719.
[50] Singleton EW, Strzeszewski J, Hadjipanayis GC. High coercivity in rapidly quenched Sm(Fe,T)12-type magnets. Appl Phys Lett. 1989;54:1934–1936.
[51] Strnat K, Hoffer G, Olson J, et al. A family of new cobalt-base permanent magnet materials. J Appl Phys. 1967;38:1001–1002.
[52] Sagawa M, Fujimura S, Togawa N, et al. New material for permanent magnets on a base of Nd and Fe (invited). J Appl Phys. 1984;55:2083–2087.
[53] Sagawa M, Fujimura S, Togawa N, et al. Permanent magnet materials based on the rare earth-iron-boron tetragonal compounds (invited). IEEE Trans Magn. 1984;MAG-20:1584–1589.
[54] Croat JJ, Herbst JF, Lee RW, et al. Pr-Fe and Nd-Fe-based materials: A new class of high-performance permanent magnets (invited). J Appl Phys. 1984; 55:2078–2082.
[55] Croat JJ, Herbst JF, Lee RW, et al. High-energy product Nd-Fe-B permanent magnets. Appl Phys Lett. 1984;44:148–149.
[56] Cadieu FJ. Recent advances in pseudobinary iron based permanent magnets. Int Mater Rev. 1995; 40:137–148.
[57] Rama Rao KVS, Markandeyulu G, Suresh KG, et al. Recent advances in 2:17 and 3:29 permanent magnet materials. Bull Mater Sci. 1999;22:509–517.
[58] Müller A. Magnetic material R,Fe,Mo,(Co) with ThMn12 structure. J Appl Phys. 1988;64:249–251.
[59] Jang TS, Stadelmaier HH. Phase equilibria and magnetic properties of iron-rich Fe-Nd-Ti and Fe-Sm-Ti alloys. J Appl Phys. 1990;67:4957–4959.
[60] Suski W. Phase diagrams as the framework of investigations of the magnetic properties of ThMn12-type f electron intermetallics. Powder Metall Met Ceram. 1997;36:231–241.
[61] Liu Y, Sellmyer DJ, Shindo D. Handbook of advanced magnetic materials. New York: Springer; 2006.
[62] Wu L, Mendoza-Garcia A, Li Q, et al. Organic phase syntheses of magnetic nanoparticles and their applications. Chem Rev. 2016;116:10473–10512.
[63] Shen B, Sun S. Chemical synthesis of magnetic nanoparticles for permanent magnet Applications. Chem Eur J. 2020;26:6757–6766.
[64] Peng S, Wang C, Xie J, et al. Synthesis and stabilization of monodisperse Fe nanoparticles. J Am Chem Soc. 2006;128:10676–10677.
[65] Hou Y, Xu Z, Peng S, et al. A facile synthesis of SmCo5 magnets from core/shell Co/Sm2O3 nanoparticles. Adv Mater. 2007;19:3349–3352.
[66] Wu Q, Cong L, Yue M, et al. A unique synthesis of rare-earth-Co-based single crystal particles by "self-aligned" Co nano-arrays. Nanoscale. 2020;12:13958–13963.
[67] Carroll KJ, Hudgins DM, Spurgeon S, et al. One-pot aqueous synthesis of Fe and Ag core/shell nanoparticles. Chem Mater. 2010;22:6291–6296.
[68] Hou Y, Xu Z, Sun S. Controlled synthesis and chemical conversions of FeO nanoparticles. Angew Chem Int Ed. 2007;46:6329–6332.
[69] Kim D, Lee N, Park M, et al. Synthesis of uniform ferrimagnetic magnetite nanocubes. J Am Chem Soc. 2009;131:454–455.
[70] Ge W, Sato R, Wu HL, et al. Simple surfactant concentration-dependent shape control of polyhedral Fe3O4 nanoparticles and their magnetic properties. ChemPhysChem. 2015;16:3200–3205.
[71] Park J, An K, Hwang Y, et al. Ultra-large-scale syntheses of monodisperse nanocrystals. Nat Mater. 2004;3:891–895.
[72] Kim J, Wu HL, Hsu S, et al. Nanoparticle approach to the formation of Sm2Fe17N3 hard magnetic particles. Chem Lett. 2019;48:1054–1057.
[73] Zhang H, Peng S, Rong C, et al. Chemical synthesis of hard magnetic SmCo nanoparticles. J Mater Chem. 2011;21:16873–16876.
[74] Shen B, Yu C, Baker AA, et al. Chemical synthesis of magnetically hard and strong rare earth metal based nanomagnets. Angew Chem Int Ed. 2019;58:602–606.
[75] Ma Z, Yue M, Liu H, et al. Stabilizing hard magnetic SmCo5 nanoparticles by N-doped graphitic carbon layer. J Am Chem Soc. 2020;142:8440–8446.
[76] Shen B, Yu C, Su D, et al. A new strategy to synthesize anisotropic SmCo5 nanomagnets. Nanoscale. 2018; 10:8735–8740.
[77] Li C, Wu Q, Ma Z, et al. A novel strategy to synthesize anisotropic SmCo5 particles from Co/Sm(OH)3 composites with special morphology. J Mater Chem C. 2018;6:8522–8527.
[78] Yue N, Li C, Wu Q, et al. A facile synthesis of anisotropic SmCo5 nanochips with high magnetic performance. Chem Eng J. 2018;343:1–7.
[79] Ali WB, Wu Q, Ma Z, et al. Chemically synthesizing PrCo5 single-crystal particles to fabricate high-performance anisotropic nanomagnets. J Magn Magn Mater. 2020;499:166205.
[80] Lee J, Hwang TY, Kang MK, et al. Synthesis of samarium–cobalt sub-micron fibers and their excellent hard magnetic properties. Front Chem. 2018;6:18.
[81] Lee J, Hwang TY, Cho HB, et al. Near theoretical ultra-high magnetic performance of rare-earth nanomagnets via the synergetic combination of calcium-reduction and chemoselective dissolution. Sci Rep. 2018;8:15656.
[82] Silva CRD, Smith S, Shim I, et al. Lanthanide(III)-doped magnetite nanoparticles. J Am Chem Soc. 2009;131:6336–6337.
[83] Yang L, Zhou Z, Liu H, et al. Europium-engineered iron oxide nanocubes with high T1 and T2 contrast abilities for MRI in living subjects. Nanoscale. 2015; 7:6843–685.
[84] Rice KP, Russek SE, Geiss RH, et al. Temperature-dependent structure of Tb-doped magnetite nanoparticles. Appl Phys Lett. 2015;106:062409.
[85] Wan H, Rong P, Liu X, et al. Morphological evolution and magnetic property of rare-earth-doped hematite nanoparticles: promising contrast agents for T1-weighted magnetic resonance imaging. Adv Funct Mater. 2017;27:1606821.
[86] Kowalik P, Mikulski J, Borodziuk A, et al. Yttrium-doped iron oxide nanoparticles for magnetic hyperthermia applications. J Phys Chem C. 2020;124:6871–6883.

[87] Chaubey GS, Poudyal N, Liu Y, et al. Synthesis of Sm–Co and Sm–Co/Fe nanocrystals by reductive annealing of nanoparticles. J Alloys Compd. 2011;509:2132–2136.
[88] Ma Z, Yang S, Zhang T, et al. The chemical synthesis of SmCo5 single-crystal particles with small size and high performance. Chem Eng J. 2016;304:993–999.
[89] Ma Z, Zhang T, Jiang C. A facile synthesis of high performance SmCo5 nanoparticles. Chem Eng J. 2015;264:610–616.
[90] Ma Z, Yue M, Wu Q, et al. Designing shape anisotropic SmCo5 particles by chemical synthesis to reveal the morphological evolution mechanism. Nanoscale. 2018;10:10377–10382.
[91] Dong Y, Zhang T, Xia X, et al. Dispersible SmCo5 nanoparticles with huge coercivity. Nanoscale. 2019;11:16962–16967.
[92] Palaka S, Yue M, Ma Z, et al. A facile chemical synthesis of PrCo5 particles with high performance. J Alloys Compd. 2020;812:151674.
[93] Tang H, Mamakhel MAH, Christensen M. Enhancing the coercivity of SmCo5 magnet through particle size control. J Mater Chem C. 2020;8:2109–2116.
[94] Okada S, Takagi K, Ozaki K. Direct preparation of submicron-sized Sm2Fe17 ultra-fine powders by reduction-diffusion technique. J Alloys Compd. 2016;663:872–879.
[95] Okada S, Suzuki K, Node E, et al. Preparation of submicron-sized Sm2Fe17N3 fine powder with high coercivity by reduction-diffusion process. J Alloys Compd. 2017;695:1617–1623.
[96] Okada S, Node E, Takagi K, et al. Synthesis of Sm2Fe17N3 powder having a new level of high coercivity by preventing decrease of coercivity in washing step of reduction diffusion process. J Alloys Compd. 2019;804:237–242.
[97] Hwang TY, Lee J, Kang MK, et al. Synthesis and magnetic properties of Sm2Co17 particles using salt-assisted spray pyrolysis and a reduction-diffusion process. Appl Surf Sci. 2019;475:986–989.
[98] Liu SF, Lin JH, Qian XL, et al. Synthesis of NdFe10Mo2 by a reduction–diffusion process. Chem Mater. 1996;8:2545–2547.
[99] Kelly BG, Unruh KM. Preparation and magnetic properties of sub-micrometer sized Sm-Co powders prepared from nanostructured precursor oxides. IEEE Trans Magn. 2013;49:3349–3352.
[100] Ma Z, Liang J, Ma W, et al. Chemically synthesized anisotropic SmCo5 nanomagnets with a large energy product. Nanoscale. 2019;11:12484–12488.
[101] Coey JMD, Sun H. Improved magnetic properties by treatment of iron-based rare earth intermetallic compounds in anmonia. J Magn Magn Mater. 1990;87: L251–L254.
[102] Sun H, Coey JMD, Gtani Y, et al. Magnetic properties of a new series of rare-earth iron nitrides: r2Fe17Ny (y ~ 2.6). J Phys Condens Matter. 1990;2:6465–6470.
[103] Otani Y, Hurley DPF, Sun H, et al. Magnetic properties of a new family of ternary rare-earth iron nitrides R2Fe17N3–δ (invited). J Appl Phys. 1991;69:5584–5589.
[104] Ogura M, Mashiyama A, Akai H. Role of N in the permanent magnet material Sm2Fe17Nx. J Phys Soc Jpn. 2015;84:084702.
[105] Christodoulou CN, Takeshita T. Nitrogenation of Sm2Fe17: mechanism, phases and stability. J Alloys Compd. 1993;202:173–182.
[106] Buschow KHJ. New developments in hard magnetic materials. Rep Prog Phys. 1991;54:1123–1213.
[107] Sato T, Ohsuna T, Yano M, et al. Permanent magnetic properties of NdFe12Nx sputtered films epitaxially grown on V buffer layer. J Appl Phys. 2017;122:053903.
[108] Hegde H, Rani R, Navarathna A, et al. Film synthesis and magnetic properties of ThMn12-type Sm(Fe1-xTx)12, x ≤ 0.12. J Appl Phys. 1991;70:6345–6347.
[109] Cadieu FJ, Hegde H, Navarathna A, et al. High-energy product ThMn12 Sm-Fe-T and Sm-Fe permanent magnets synthesized as oriented sputtered films. Appl Phys Lett. 1991;59:875–877.
[110] Sepehri-Amin H, Tamazawa Y, Kambayashi M, et al. Achievement of high coercivity in Sm(Fe0.8Co0.2)12 anisotropic magnetic thin film by boron doping. Acta Materialia. 2020;194:337–342.
[111] Dirba I, Li J, Sepehri-Amin H, et al. Anisotropic, single-crystalline SmFe12-based microparticles with high roundness fabricated by jet-milling. J Alloys Compd. 2019;804:155–162.
[112] Dirba I, Sepehri-Amin H, Ohkubo T, et al. Development of ultra-fine grain sized SmFe12-based powders using hydrogenation disproportionation desorption recombination process. Acta Materialia. 2019;165:373–380.
[113] Dirba I, Harashima Y, Sepehri-Amin H, et al. Thermal decomposition of ThMn12-type phase and its optimum stabilizing elements in SmFe12-based alloys. J Alloys Compd. 2020;813:152224.
[114] Harashima Y, Terakura K, Kino H, et al. First-principles study on stability and magnetism of NdFe11M and NdFe11MN for M = Ti, V, Cr, Mn, Fe, Co, Ni, Cu, Zn. J App Phys. 2016;120:203904.
[115] Chen NX, Hao SQ, Wu Y, et al. Phase stability and site preference of Sm(Fe,T)12. J Magn Magn Mater. 2001;233:169–180.
[116] Moze O, Pareti L, Solzi M, et al. Neutron diffraction and magnetic anisotropy study of Y-Fe-Ti intermetallic compounds. Solid State Commun. 1988;66:465–469.
[117] Matsumoto M, Hawai T, Ono K. (Sm, Zr)Fe12–xMx (M = Zr, Ti, Co) for permanent-magnet applications: Ab initio material design integrated with experimental characterization. Phys Rev Appl. 2020;13:064028.
[118] Suzuki S, Kuno T, Urushibata K, et al. A (Nd, Zr)(Fe, Co)11.5Ti0.5Nx compound as a permanent magnet material. AIP Adv. 2014;4:117131.
[119] Sakuma N, Suzuki S, Kuno T, et al. Influence of Zr substitution on the stabilization of ThMn12–type (Nd1–αZrα)(Fe0.75Co0.25)11.25Ti0.75N1.2–1.4 (α = 0–0.3) compounds. AIP Adv. 2016;6:056023.
[120] Gjoka M, Psycharis V, Devlin E, et al. Effect of Zr substitution on the structural and magnetic properties of the series Nd1–xZrxFe10Si2 with the ThMn12 type structure. J Alloys Compd. 2016;687:240–245.
[121] Kobayashi K, Suzuki S, Kuno T, et al. The stability of newly developed (R,Zr)(Fe,Co)12–xTix alloys for permanent magnets. J Alloys Compd. 2017;694:914–920.
[122] Hagiwara M, Sanada N, Sakurada S. Effect of Y substitution on the structural and magnetic properties of Sm(Fe0.8Co0.2)11.4Ti0.6. J Magn Magn Mater. 2018;465:554–558.
[123] Kuno T, Suzuki S, Urushibata K, et al. (Sm,Zr)(Fe,Co) 11.0–11.5Ti1.0–1.5 compounds as new permanent magnet materials. AIP Adv. 2016;6:025221.
[124] Kuno T, Suzuki S, Urushibata K, et al. Coercivity of pulverized ThMn12 compounds with a limited amount of α-(Fe,Co) phase. Mater Trans. 2019;60:1697–1706.
[125] Tozman P, Takahashi YK, Sepehri-Amin H, et al. The effect of Zr substitution on saturation magnetization in

(Sm1–xZrx)(Fe0.8Co0.2)12 compound with the ThMn12 structure. Acta Materialia. 2019;178:114–121.
[126] Harashima Y, Fukazawa T, Kino H, et al. Effect of R-site substitution and the pressure on stability of RFe12: A first-principles study. J Appl Phys. 2018; 124:163902.
[127] Kobayashi K, Furusawa D, Suzuki S, et al. High-temperature stability of ThMn12 magnet materials. Mater Trans. 2018;59:1845–1853.
[128] Miyake T, Terakura K, Harashima Y, et al. First-principles study of magnetocrystalline anisotropy and magnetization in NdFe12, NdFe11Ti, and NdFe11TiN. J Phys Soc Jpn. 2014;83:043702.
[129] Harashima Y, Terakura K, Kino H, et al. Nitrogen as the best interstitial dopant among X = B, C, N, O, and F for strong permanent magnet NdFe11TiX: first-principles study. Phys Rev B. 2015;92:184426.
[130] Hadjipanayis GC, Gabay AM, Schönhöbel AM, et al. ThMn12-type alloys for permanent magnets. Engineering. 2020;6:141–147.
[131] Su MZ, Liu SF, Qian XL, et al. An alternative approach to the finely crystalline powder of rare earth–transition metal alloys. J Alloys Compd. 1997;249:229–233.
[132] Cheng QM, Lin JH, Su MZ. On structural and magnetic properties of ErFe11WZx, (Z = H, N). Solid State Commun. 1998;106:455–458.
[133] Cheng QM, Lin JH, Su MZ. On the synthesis and magnetic properties of LnFe10Si2Zx (Z=N, H and Ln=Tb, Er). J Alloys Compd. 1998;269:297–300.
[134] Cheng QM, Lin JH, Su MZ. On synthesis and magnetic properties of YFe10Si2Zx (Z=H and N). J Alloys Compd. 1998;275–277:6–9.
[135] Cheng QM, Lin JH, Su MZ. On Synthesis and Magnetic Properties of Nd(Fe, Mo, Ti)12Zx (Z=N, H). J Alloys Compd. 1998;280:310–313.
[136] Cheng QM, Lin JH, Su MZ. On the synthesis and magnetic properties of Nd(Fe,Mo,Ti)12. App Phys Lett. 1998;73:2500–2502.
[137] Christodoulou CN, Takeshita T. Preparation, structural and magnetic properties and stability of interstitial Sm2Fe17-carbonitrohydrides. J Alloys Compd. 1993;198:1–24.
[138] Christodoulou CN, Komada N. High coercivity anisotropic Sm2Fe17N3 powders. J Alloys Compd. 1995;222:92–95.
[139] Isnard O, Guillot M, Miraglia S, et al. High field magnetization measurements of SmFe11Ti and SmFe11TiH1−δ. J Appl Phys. 1996;79:5542–5544.
[140] Isnard O, Miraglia S, Guillot M, et al. Hydrogen effects on the magnetic properties of RFe11Ti compounds. J Alloys Compd. 1998;275–277:637–641.
[141] Morales M, Bacmann M, Wolfers P, et al. Impact of hydrogen and carbon insertion on the fundamental characteristics of ErMn12–xFex compounds. J Magn Magn Mater. 2001;236:83–92.
[142] Isnard O. Influence of hydrogen insertion on the magnetic properties of the RFe11Ti phases. J Alloys Compd. 2003;356–357:17–21.
[143] Piquer C, Grandjean F, Isnard O, et al. A magnetic and Mössbauer spectral study of the spin reorientation in NdFe11Ti and NdFe11TiH. J Appl Phys. 2004;95:6308–6316.
[144] Isnard O, Pop V. Effect of hydrogen as interstitial element on the magnetic properties of some iron rich intermetallic compounds. J Alloys Compd. 2011;509S:S549–S554.
[145] Tereshina IS, Nikitin SA, Pankratov NY, et al. Magnetic anisotropy of LuFe11Ti compound and its hydride and nitride. J Magn Magn Mater. 2001;231:213–218.
[146] Tereshina IS, Pankratov NY, Tereshina EA, et al. Magnetocrystalline anisotropy of hydrogenated and nitrogenated rare-earth intermetallic compound SmFe11Ti. Phys Met Metall. 2005;99:S46–S49.
[147] Tereshina IS, Kostyuchenko NV, Tereshina-Chitrova EA, et al. ThMn12-type phases for magnets with low rare-earth content: crystal-field analysis of the full magnetization process. Sci Rep. 2018;8:3595.
[148] Kneller EF, Hawig R. The exchange-spring magnet: a new material principle for permanent magnets. IEEE Trans Magn. 1991;27:3588–3600.
[149] Skomski R, Coey JMD. Giant energy product in nanostructured two-phase magnets. Phys Rev B. 1993;48:15812–15816.
[150] O'Donnell K, Coey JMD. Characterization of hard magnetic two-phase mechanically alloyed Sm2Fe17N3/α-Fe nanocomposites. J Appl Phys. 1997;81:6310–6321.
[151] Schrefl T, Fischer R, Fidler J, et al. Two- and three-dimensional calculation of remanence enhancement of rare-earth based composite magnets (invited). J Appl Phys. 1994;76:7053–7058.
[152] Zeng H, Li J, Liu JP, et al. Exchange-coupled nanocomposite magnets by nanoparticle self-assembly. Nature. 2002;420:395–398.
[153] Yu L, Yang C, Hou Y. Controllable Nd2Fe14B/α-Fe nanocomposites: chemical synthesis and magnetic properties. Nanoscale. 2014;6:10638–10642.
[154] Yu LQ, Zhang YP, Yang Z, et al. Chemical synthesis of Nd2Fe14B/Fe3B nanocomposites. Nanoscale. 2016;8:12879–12882.
[155] Hou Y, Sun S, Rong C, et al. SmCo5/Fe nanocomposites synthesized from reductive annealing of oxide nanoparticles. Appl Phys Lett. 2007;91:153117.
[156] Shen B, Mendoza-Garcia A, Baker SE, et al. Stabilizing Fe nanoparticles in the SmCo5 matrix. Nano Lett. 2017;17:5695–5698.
[157] Yang C, Jia L, Wang S, et al. Single domain SmCo5@Co exchange-coupled magnets prepared from core/shell Sm[Co(CN)6]□4H2O@GO particles: a novel chemical approach. Sci Rep. 2013;3:3542.
[158] Ma Z, Zhang T, Jiang C. Exchange-coupled SmCo5/Co nanocomposites synthesized by a novel strategy. RSC Adv. 2015;5:89128–89132.
[159] Teranishi T, Wachi A, Kanehara M, et al. Conversion of anisotropically phase-segregated Pd/γ-Fe2O3 nanoparticles into exchange-coupled fct-FePd/α-Fe nanocomposite magnets. J Am Chem Soc. 2008;130:4210–4211.
[160] Sakuma N, Ohshima T, Shoji T, et al. Exchange coupling interaction in L10-FePd/α-Fe nanocomposite magnets with large maximum energy products. ACS Nano. 2011;5:2806–2814.
[161] Matsumoto K, Sato R, Trinh TT, et al. Formation of strong L10-FePd/α-Fe nanocomposite magnets by visualizing efficient exchange coupling. Nanoscale Adv. 2019;1:2598–2605.
[162] Balasubramanian B, Mukherjee P, Skomski R, et al. Magnetic nanostructuring and overcoming Brown's paradox to realize extraordinary high-temperature energy products. Sci Rep. 2014;4:6265.
[163] Liu X, He S, Qiu JM, et al. Nanocomposite exchange-spring magnet synthesized by gas phase method: from isotropic to anisotropic. Appl Phys Lett. 2011;98:222507.

[164] Takagi K, Nakayama H, Ozaki K, et al. Fabrication of high-performance Sm–Fe–N isotropic bulk magnets by a combination of high-pressure compaction and current sintering. J Magn Magn Mater. 2012;324:1337–1341.

[165] Ogawa D, Xu XD, Takahashi YK, et al. Emergence of coercivity in Sm(Fe0.8Co0.2)12 thin films via eutectic alloy grain boundary infiltration. Scr Mater. 2019; 164:140–144.